Correspondence to:

P. Cordier,
patrick.cordier@univ-lille.fr

Evidence of Dislocation Mixed Climb in Quartz From the Main Central and Moine Thrusts: An Electron Tomography Study

Timmo Weidner[1], Alexandre Mussi[1] (ID), **Olivier Castelnau[2]** (ID), **Andreas Kronenberg[3], Richard Law[4]** (ID)**, and Patrick Cordier[1,5]** (ID)

[1]Univ. Lille, CNRS, INRAE, Centrale Lille, UMR 8207 - UMET – Unité Matériaux et, Transformations, Lille, France, [2]Laboratoire PIMM, Arts et Métiers Institute of Technology, CNRS, Cnam, Paris, France, [3]Department of Geology and Geophysics, Texas A&M University, College Station, TX, USA, [4]Department of Geosciences, Virginia Tech, Blacksburg, VA, USA, [5]Institut Universitaire de France, Paris, France

Abstract In this study we apply electron tomography to characterize 3D dislocation microstructures in two quartz mylonite specimens from the Moine and Main Central Thrusts, both of which accommodated displacements by dislocation creep in the presence of water. Both specimens show dislocation activity with dislocation densities of the order of 3–4×10^{12} m^{-2} and evidence of recovery from the presence of subgrain boundaries. $\langle a \rangle$ slip occurs predominantly on pyramidal and prismatic planes ($\langle a \rangle$ basal glide is not active). [c] Glide is not significant. On the other hand, we observe a very high level of activation of $\langle c + a \rangle$ glide on the $\{10\bar{1}0\}$, $\{10\bar{1}1\}$, $\{11\bar{2}n\}$ ($n = 1,2$) and even $\{21\bar{3}1\}$ planes. Approximately 60% of all dislocations show evidence of climb with a predominance of mixed climb, a deformation mechanism characterized by dislocations moving in a plane intermediate between the glide and the climb planes. This atypical mode of deformation demonstrates comparable glide and climb efficiency under natural deformation conditions. It promotes dislocation glide in planes not expected for the quartz structure, probably by inhibiting lattice friction. Our quantitative characterization of the microstructure enables us to assess the strain that dislocations can generate. We show that glide systems indicated by the observed dislocations are sufficient to accommodate any arbitrary 3D strain by themselves. Although historically dislocation glide has been regarded as being primarily responsible for producing strain, activation of climb can also directly contribute to the finite strain. On the basis of this characterization, we propose a numerical modeling approach for attempting to characterize the local stress state that gave rise to the observed microstructure.

Plain Language Summary In this study, we characterize dislocation microstructures generated in quartz deformed in natural shear zones by advanced transmission electron microscopy to better understand the geological deformation conditions and the response of quartz to applied stresses. We characterize the crystal defects responsible for deformation of the mineral and their three-dimensional geometries. We highlight an original deformation mechanism activated at very low natural strain rates that involves simultaneous dislocation glide and climb outside of their crystallographic glide planes.

1. Introduction

Quartz is one of the major constituents of the Earth's continental crust. Above *ca*. 300°C (corresponding to depths beyond 10 km, Stipp et al., 2002a), quartz is ductile and it appears to be one of the weaker minerals in naturally deformed rocks of the continental crust. The plasticity of quartz is thus important to the description of the rheology of the lower crust. Many studies over the last 60 years have been devoted to the plasticity of quartz. Still, the plastic behavior of this mineral is only partially understood, even in the laboratory. Our understanding of the crystal plasticity of this mineral under natural conditions, and its control of crustal rheology, is far from resolved. The simple question of how quartz deforms by glide of dislocations is not straightforward. In this trigonal mineral (Figure 1), glide of $\langle a \rangle$ dislocations ($1/3 \langle 2\bar{1}\bar{1}0 \rangle$) in the basal plane is expected (Baëta & Ashbee, 1969). It was indeed observed experimentally very early on and is complemented at higher temperatures by glide of [c] ([0001]) dislocations in prismatic planes (Blacic, 1975). However, these slip systems by themselves are insufficient to satisfy the von Mises-Taylor criterion for general strains with arbitrary non-zero components (von Mises, 1928; Taylor, 1938; Ball & White, 1978). Activating $\langle c + a \rangle$ glide can potentially satisfy the remaining strain components (Baëta & Ashbee, 1969; Trépied & Doukhan, 1982): however, this mechanism seems to have

Writing – original draft:
Timmo Weidner, Alexandre Mussi,
Olivier Castelnau, Andreas Kronenberg,
Richard Law, Patrick Cordier
Writing – review & editing:
Timmo Weidner, Alexandre Mussi,
Olivier Castelnau, Andreas Kronenberg,
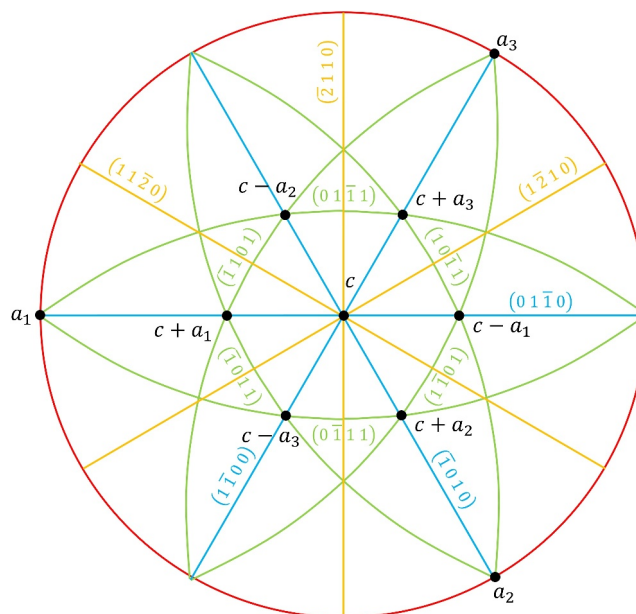Richard Law, Patrick Cordier

Figure 1. Representation on equal-angle Wulff net, upper hemisphere, of crystallographic planes and directions usually reported for the glide systems in the quartz structure. Three $\langle a \rangle$ directions (the notation "$\langle\ \rangle$" stands for equivalent directions where "[ ]" is used for a specific direction) can induce glide in the (0001) basal plane (the great circle in red): $a_1 = 1/3[2\bar{1}\bar{1}0]$, $a_2 = 1/3[\bar{1}2\bar{1}0]$ and $a_3 = 1/3[\bar{1}\bar{1}20]$. The $[c] = [0001]$ dislocations can glide in first-order $\{10\bar{1}0\}$ (in blue), or second-order $\{2\bar{1}\bar{1}0\}$ (in orange), prismatic planes. Here, "$\{\ \}$" notation is applied to equivalent planes, while a particular plane is designated by "( )". $\langle c + a \rangle = 1/3\langle 2\bar{1}\bar{1}3 \rangle$ dislocations are usually reported to glide in rhombohedral $\{10\bar{1}1\}$ planes (in green).

been neglected for several years. As far as deformation involving dislocation motion is concerned, conservative glide is not the only process contributing to creep. Additional degrees of freedom to deformation may be facilitated by dislocation climb as point defects become mobile through diffusion. Strains may also be satisfied by cracking at low effective stresses or sliding at grain boundaries (Behrmann & Mainprice, 1987; Fliervoet et al., 1997; Fukuda et al., 2018; Rutter & Brodie, 2004; Tokle et al., 2019).

Beyond the fundamental questions about intracrystalline deformation mechanisms that apply to all minerals (and crystalline solids in general), dislocation creep of quartz and its mechanical properties depend on impurities, particularly those derived from water (such as hydroxyls at structural sites of the crystalline structure and dislocations). Owing to the three-dimensional network of strong Si-O bonds, dry quartz is very strong, and almost undeformable by dislocation motions in the laboratory. In contrast, quartz deformed at tectonic strain rates in the presence of water (at temperatures greater than 300°C) is ductile and appears to be one of the weakest minerals of quartzo-feldspathic crustal rocks.

The phenomenon of water (or hydrolytic) weakening was discovered by Griggs and Blacic (1965) and interpreted to result from hydrolysis of strong Si-O-Si bonds, to form weak hydrogen-bonded SiOH groups at dislocation cores (Griggs, 1967, 1974). Hydrous defects were originally thought to be transported to dislocation cores by volume diffusion. However, alternative water weakening models have since been proposed, including potential effects of hydrogen impurities on other charged point defects that facilitate climb (Hobbs, 1981, 1984), and effects of hydrogen impurities on concentrations (and mobilities) of dislocation kinks and jogs (Hirsch, 1981). All of these models have been challenged, though, by the discovery that solubilities of OH defects within the quartz structure are low (Cordier & Doukhan, 1989, 1991; Doukhan & Paterson, 1986; Kronenberg et al., 1986), limiting the predicted changes in point defect chemistry of crystalline quartz and the delivery of OH to dislocations cores by radial volume diffusion to dislocation cores. Ab initio models of hydrous molecular structures and dislocation kinks in quartz indicate that hydrous defects are stable at dislocation cores, particularly at dislocation kinks (Heggie et al., 1985; Heggie & Jones, 1986). Hydrous defects are therefore thought to gain access to dislocation cores by pipe diffusion from grain boundaries or fluid inclusions (Bakker & Jansen, 1990, 1994; Cordier & Doukhan, 1989, 1991; Cordier et al., 1988; Heggie, 1992).

Hydrolytic weakening has only been observed when measured OH concentrations are supersaturated with respect to hydrous defect solubilities (Cordier & Doukhan, 1989; Kekulawala et al., 1978, 1981; Kirby & McCormick, 1979). Initial transient creep rates of OH-supersaturated quartz have been explained by mechanisms of dislocation nucleation at non-equilibrium water clusters and fluid inclusions with further dislocation multiplication facilitated by pipe diffusion of hydrous defects (Cordier & Doukhan, 1989; Gerretsen et al., 1989; McLaren et al., 1989). Most relevant to the present study is the role of hydrous defects in facilitating dislocation climb during plastic deformation of quartz.

Dislocation climb is usually regarded as a recovery mechanism rather than a strain-producing mechanism (Tullis & Yund, 1989). However, activation of the climb mechanism proposed by Nabarro (1967) was suggested by Ball and White (1978) and Ball and Glover (1979) to apply to quartz single crystals experimentally compressed along the [0001] direction. The activity of dislocation climb in quartz also has implications for the onset of dynamic recrystallization (Hirth & Tullis, 1992). In the absence of significant contributions from dislocation climb at low temperature, recrystallization involves strain-induced grain boundary migration (GBM), or bulging. At higher temperature, when dislocation climb is enhanced, recrystallization may occur by progressive subgrain rotation (Hirth & Tullis, 1992).

In a recent study, we applied an analytical method to quartz using electron tomography of dislocation microstructures to determine the components of the plastic strain tensor (Mussi, Gallet et al., 2021) resulting from the displacement of these dislocations. This study revealed the unexpected activation of climb of $\langle c + a \rangle$ dislocations. The present study was undertaken to learn whether climb of $\langle c + a \rangle$ dislocations is important to the plastic deformation of quartz in natural shear zones. Quartz mylonite specimens were selected for electron tomography from the Moine and Main Central Thrusts (MCTs), both of which deformed extensively by dislocation creep in the presence of water. Transmission electron microscopy (TEM) tomography of dislocations presented in this study is applied to determine the relative mobilities of dislocations by glide and climb.

2. Materials and Methods

2.1. Specimens

Two quartz mylonite specimens have been chosen for this study, which exhibit optical microstructures and crystallographic preferred orientations due to dislocation creep and dynamic recrystallization. Both mylonites come from major shear zones of collisional tectonic boundaries, one from the MCT of Northwest India, associated with the southward-directed Oligocene-Miocene extrusion of the Greater Himalayan slab (Hodges, 2000) and the other from the gently SE-dipping Moine Thrust (MT) of Northwest Scotland, associated with Caledonian shortening of the foreland continental margin during closure of the Iapetus Ocean (Strachan et al., 2002). The MCT mylonite specimen S-09-35a (hereafter referred to as MCT) was collected from a quartz-rich horizon of Greater Himalayan orthogneisses exposed in the western part of the Sutlej Valley, at a structural distance of 71 m above the MCT (Law et al., 2013). The MT mylonite specimen SG-10 (hereafter referred to as MT) was collected from Cambrian quartzites of the footwall exposed at the Stack of Glencoul, just 4.6 m below the thrust contact with overlying Neoproterozoic Moine schists (Christie, 1963; Law et al., 1986, 2010). It was in these quartz mylonites that recrystallization (rather than brittle fracturing) was first recognized and explicitly named as a grain scale deformation process leading to grain size reduction in naturally deformed high strain rocks (Christie, 1960; Christie et al., 1954) and directly correlated with intracrystalline slip and recrystallization microstructures produced in experimentally deformed quartz-rich rocks (Carter et al., 1964, their Plate 9; see review by Law & Johnson, 2010).

The MCT specimen is made up of highly sheared quartz horizons within a sheared orthogneiss matrix of mixed quartz and layer silicates (Figure 2). Almost all quartz horizons of this specimen have been recrystallized, but the TEM observations made here are from larger residual quartz grains whose deformation gives them the grain shapes of augen (Figure 2). These quartz augen exhibit patchy undulatory extinction and well-developed subgrain walls. Fine recrystallized quartz grains appear within the larger grains and at their margins, with microstructures that indicate that recrystallization occurred predominantly by subgrain rotation (SGR) with subordinate grain boundary migration (GBM) (Law et al., 2013; Stipp et al., 2002b). The mean recrystallized grain size measured in the quartz-rich layers is ~45 µm (Francsis, 2012). Crystallographic c-axes of recrystallized quartz-rich horizons show distinctly asymmetric cross-girdle patterns due to internal shear in the fault transport direction, with high
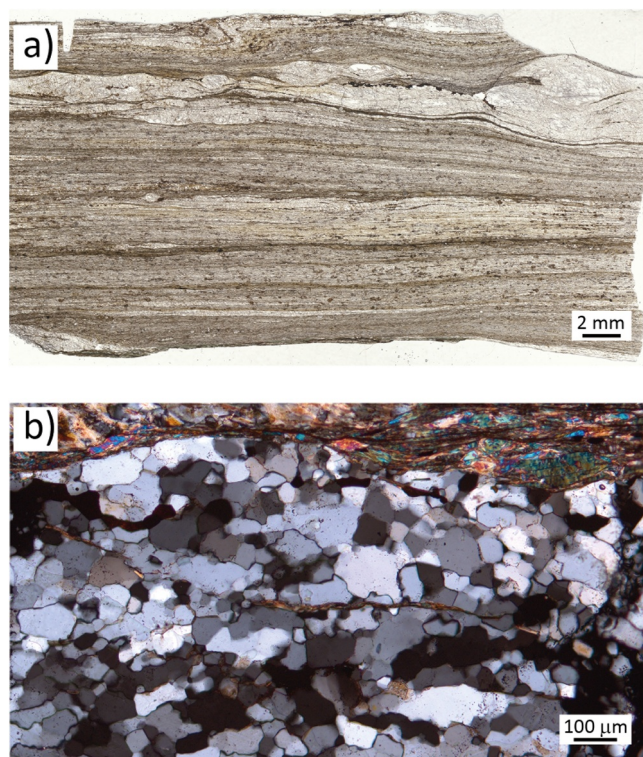
Figure 2. Low magnification optical micrographs of specimen Main Central Thrust (MCT) (S-09-35a) from hanging wall orthogneisses of the MCT, collected from the western part of the Sutlej Valley, NW India (Law et al., 2013): (a) Plane light image of XZ section prepared perpendicular to foliation (horizontal in this image) and parallel to lineation (in foliation), nearly parallel to the fault transport direction (top to the left), with sheared quartz horizons within a matrix of quartz and layer silicates. (b) Deformation and recrystallization microstructures of quartz horizon in cross-polarized light.

c-axis densities defining a great circle consistent with oblique grain shape alignments subparallel to lineation and top-to-the SW (thrust) shear (Law et al., 2013).

Using the Faleiros et al. (2016) opening angle thermometer, the temperature of deformation for MCT is estimated to be 515°C, based on a measured c-axis fabric opening angle of 68° (Law et al., 2013). In contrast to the differences in crystal fabric and petrologically based temperatures of MT specimens at the Stack of Glencoul, estimates of peak deformation and metamorphic temperatures, based on c-axis patterns and coexisting garnet and muscovite compositions of mylonites collected from the Sutlej Valley, are in close agreement. Peak pressures estimated for mylonites ~1,100 m structurally above MCT are of the order of 800 MPa (Supplementary file in Law et al., 2013). The differential stress estimated from the mean recrystallized grain size of MCT and the modified Stipp et al. (2006) grain size piezometer (with the adjustment of Holyoke & Kronenberg, 2010) is ~24 MPa (Francsis, 2012; Law et al., 2013). The strain rate predicted by the Hirth et al. (2001) flow law at these conditions is $\sim 10^{-12}$ s^{-1}.

Other than our own preliminary TEM of MCT samples, we are not aware of any previous studies of dislocations by electron microscopy of high strain rocks from the Sutlej Valley. Undulatory extinction and subgrains of the MCT sample at the optical scale correspond to dislocations and subgrain walls at the TEM observational scale. Infrared absorption measurements of OH bands in MCT reveal large but variable OH contents of large augen quartz grains with mean molar OH contents of 3,010 (±2,780) ppm (Kronenberg et al., 2017). These bands are due to intragranular molecular water, and TEM shows that fine fluid inclusions routinely decorate dislocations.

The MT specimen consists of sheared ribbon (high aspect ratio) quartz grains with smooth undulatory extinction observed in conventional thin sections, and well-developed subgrain walls that are apparent in ultra-thin sections (~5 µm) (Kronenberg et al., 2020), consistent with optical microscopy of etched sections and TEM of nearby mylonitic Cambrian quartzites (Ord & Christie, 1984; Weathers et al., 1979). Ribbon quartz grains are recrystallized at their margins, with microstructures due to grain boundary bulging (BLG) and subordinate subgrain rotation (SGR) (Law, 2014; Stipp et al., 2002b); over 70% of this specimen consists of recrystallized grains (with a 21 µm mean size; Weathers et al., 1979; Kronenberg et al., 2020) but the new TEM observations of this study are from original ribbon quartz grains (Figure 3). Crystallographic c-axes of ribbon and recrystallized quartz grains exhibit nearly symmetric crossed-girdle patterns aligned with respect to grain shape foliation and lineation (Law et al., 2010), consistent with significant plane-strain foliation-normal shortening by glide on multiple slip systems with Burgers vectors parallel to ⟨a⟩ and to [c] (and other crystallographic slip vectors with components in a and c).

The temperature of deformation for the leading edge of the MT, based on crystallinity of white micas, is relatively low, 300–350°C (Johnson et al., 1985), while temperature estimates for the MT specimen based on opening angles of quartz c-axis fabrics measured on ribbon detrital quartz grains (53°) and matrix recrystallized quartz grains (69°) are as high as 415°C and 525°C respectively (Law et al., 2010; Faleiros et al., 2016 opening angle thermometer). Peak lithostatic pressures during mylonitization have not been determined. The differential stress estimated from the mean recrystallized grain size (21 µm) of MT and the modified Stipp et al. (2006) recrystallized grain size piezometer (with the adjustment of Holyoke & Kronenberg, 2010) is ~44 MPa, and strain rates based on this stress, temperature estimates of 350–400°C, and the quartzite flow law of Hirth et al. (2001) are between 10^{-14} s^{-1} and 10^{-13} s^{-1}.

Preliminary TEM observations of MT corroborate earlier observations of dislocation microstructures (Ord & Christie, 1984; Weathers et al., 1979) and intimate dislocation-fluid inclusion relationships suggest that hydrogen defects had direct access to the cores of dislocations. Infrared absorption measurements of OH bands of original
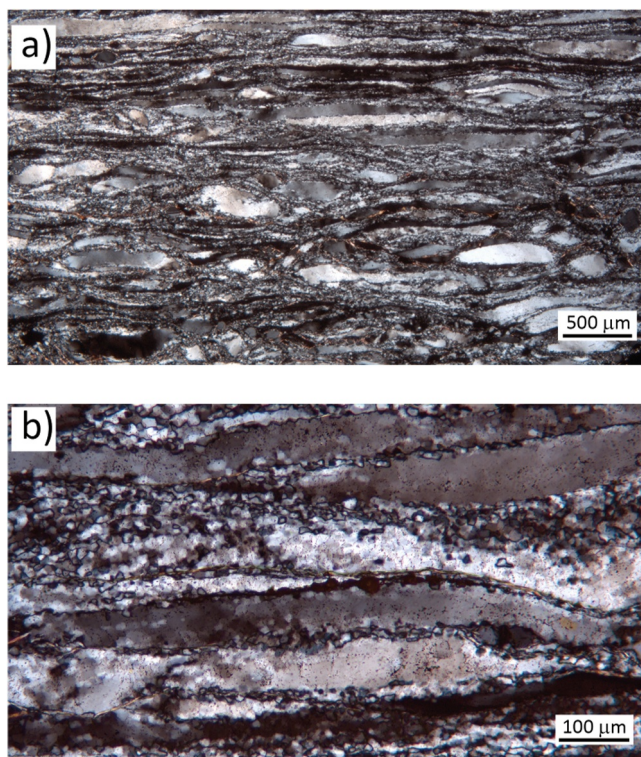
Figure 3. Optical micrographs of specimen Moine Thrust (MT) (SG-10) from footwall quartz mylonites of the MT collected at the Stack of Glencoul, NW Scotland (Christie, 1963; Law, 2014; Law et al., 1986, 2010): (a) Cross-polarized image of XZ section prepared perpendicular to foliation (horizontal in this image) and parallel to lineation (in foliation) and fault transport direction (top to the left) shows highly sheared (high aspect ratio) ribbon quartz grains and extensive dynamic recrystallization. (b) Larger ribbon quartz grains show smoothly undulatory extinction with serrated grain boundaries at their margins, of similar dimensions as recrystallized quartz grains.

ribbon quartz grains of MT are large, varying from one grain to another, with molar OH/Si concentrations of 2,400 ($\pm$700) ppm (H/10^6 Si) (Kronenberg et al., 2020).

While the inferred temperatures, pressures, differential stresses and strain rates of the two mylonite specimens investigated in this study vary, the overall crystallographic fabrics are remarkably similar. With their similar quartz cross-girdle c-axis fabrics and fabric opening angles for the MCT and MT specimens (68° for recrystallized grains in MCT, and 53° and 69° measured for deformed detrital and recrystallized grains, respectively, in MT) we might expect similar dislocation slip systems to be important with similar proportions of slip vector components in the a and c directions.

Temperature estimates for these specimens correspond well with the temperature ranges for dynamic recrystallization of quartz by BLG, SGR, and GBM mechanisms (Stipp et al., 2002a, 2002b); subgrain rotation recrystallization appears to be important for both mylonites, with the implication that dislocation climb is important in both tectonic settings and deformation conditions. In addition to SGR recrystallization, the MCT specimen has grain boundaries characteristic of some GBM recrystallization, while the MT specimen exhibits evidence for BLG recrystallization as well as the SGR mechanism (Kronenberg et al., 2017, 2020).

2.2. Transmission Electron Microscopy

Dislocation Electron Tomography (DET) reconstructs in 3D the dislocation microstructure (Barnard et al., 2006). This method differs from that of conventional tomography studies, since DET is based on diffraction contrast. Dislocations in the specimens MCT and MT zone are imaged using the high-structure factor $11\bar{2}2$ and $1\bar{1}01$ diffraction vectors, respectively. DET requires precise alignment of the diffraction vectors along the tilt axis (with an accuracy of $\pm 0.1°$) in order to maintain constant diffraction contrast conditions for images acquired over the entire tilt series. Once this key alignment is satisfied, a tilt-series of images is acquired, capturing several micrographs of the region of interest for numerous tilt angles (generally consisting of approximately 60 projected images acquired over every two degrees of tilt). DET analyses were carried out using the electron microscopy facility of the Advanced Characterization Platform of the Chevreul Institute (University of Lille), with a FEI® Tecnai $G^2$20Twin microscope, operating at 200 kV equipped with a LaB$_6$ filament. TEM analyses were conducted with a high-angle triple-axis sample-holder (Hata et al., 2011) with a maximal angular range of $\pm 80°$ in weak-beam dark-field (WBDF) and with a conventional double-tilt sample-holder with a maximal angular range of $\pm 60°$ in bright-field conditions. As quartz is known to be electron beam sensitive, special precautions were taken during acquisition:

- TEM analyses were performed with a small condenser aperture of 100 µm in diameter and a small spot size of 11.3 nm in diameter.
- To highly enhance the WBDF micrographs signal-to-noise ratio, without increasing the electron dose, pixels have been gathered four by four.
- Last but not least, tilt-series were acquired with fewer projected images than normally employed in DET (less than 30 micrographs), before much electron beam damage was observed.

For the MCT specimen, WBDF micrographs were acquired every 5° from −55° to 70° (tilt-series composed of 26 projected images), and for the MT specimen, bright-field micrographs were acquired every 10° from −50° to 50° and for −45°–35° (tilt-series composed of 11 and 9 projected images respectively). Relations between the crystal reference system and the specimen reference system were obtained simulating electron diffraction patterns with the "Electron Diffraction" software from Morniroli et al. (1994). Since dislocation contrast is intrinsically weak in
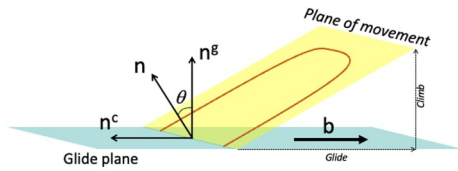
Figure 4. Geometry of a dislocation in mixed climb configuration that is where the plane of movement (identified by its normal **n**) is intermediate between the glide plane and the climb plane. $\mathbf{n}^g$ is the normal of the dislocation glide plane, $\mathbf{n}^c$ is the normal of the dislocation climb plane. **b** is the Burgers vector.

WBDF mode, the tilt-series alignment must be conducted manually with one-pixel accuracy employing Gatan® image alignment software. Each WBDF micrograph was numerically filtered with the background subtraction option of ImageJ software, to enhance the dislocation contrast of the tilt-series obtained with an intermediate number of projected images (26 micrographs). Given that the tilt-series for quartz was obtained with relatively few projected images (9 and 11 bright-field micrographs), each dislocation of each micrograph was redrawn to consider only the position of the dislocation line (following the analytical method of Mussi, Gallet et al., 2021). Image reconstruction was conducted using the Weighted Back Projection (WBP) algorithm (Herman et al., 1976), based on the Radon transformation. The WBP algorithm is freely available with the TomoJ plugin (Messaoudi et al., 2007) accessible in ImageJ. This reconstruction generates a volume which is interpolated in the angular range of acquisition and extrapolated in the missing-wedge. This method leads to ribbon shapes of the reconstructed dislocations (thin dislocation widths in the acquisition angular range and thick dislocation widths in the missing-wedge). The UCSF Chimera free software (Pettersen et al., 2004) is used to redraw the dislocations in the volume which re-establishes the cylindrical geometries of the dislocations (Liu & Robertson, 2011; Mussi et al., 2016). The procedure for producing 3D DET volumes is summarized in the supplements and illustrated using the Supplementary Movies S3–S7.

2.3. Burgers Vector Indexing Method

Burgers vector identifications were conducted using the invisibility criterion $\mathbf{g} \cdot \mathbf{b} = 0$, where $\mathbf{g}$ is the considered diffraction vector and $\mathbf{b}$ is the Burgers vector. Dislocation intensity has also been used for indexing, knowing that the peak value of the dislocation intensity in weak-beam conditions is assumed to be approximately proportional to $(\mathbf{g} \cdot \mathbf{b})^2$ (De Ridder & Amelinckx, 1971). The thickness fringe method developed by Ishida et al. (1980) was also used to index Burgers vectors in order to reduce the necessary number of micrographs required for our analyses. This technique consists of counting the number of thickness fringes observed for dislocations that intersect thin foil surfaces (this number corresponds to the $|\mathbf{g} \cdot \mathbf{b}|$ product). Consequently, just three independent diffraction conditions were sufficient for Burgers vector characterization.

2.4. Potential Plastic Strain Associated With Dislocation Segments

Most of the dislocation segments observed in this study lie out of their glide planes. This configuration is discussed in Section 4.3. These dislocation segments must be analyzed, recognizing that they must have moved by a combination of glide and climb. In the following, we express the strain that can be generated by the displacement of the dislocation segments present in the specimen, taking into account their movement plane. The geometry is represented schematically in Figure 4. We denote **n** the unit vector normal to the plane containing the dislocation line (referred to as the movement plane), and $\mathbf{n}^g$ the unit vector normal to the glide plane (index.^{g} stands for "glide"). The Burgers vector **b** is thus perpendicular to $\mathbf{n}^g$ (Figure 4). The unit line vector of the dislocation, denoted **l**, is in the movement plane and is therefore perpendicular to **n**. For the part of a segment that is edge oriented, the line vector, denoted $\mathbf{l}^e$ (index.^{e} stands for "edge") is also perpendicular to the Burgers vector. Therefore, it can be expressed as

$$\mathbf{l}^e = \frac{\mathbf{b} \times \mathbf{n}}{\|\mathbf{b} \times \mathbf{n}\|} \tag{1}$$

where "$\times$" is the cross product. The normal $\mathbf{n}^g$ of the dislocation glide plane is perpendicular to both the line vector $\mathbf{l}^e$ and the Burgers vector **b** and can thus be written

$$\mathbf{n}^g = \frac{\mathbf{l}^e \times \mathbf{b}}{\|\mathbf{l}^e \times \mathbf{b}\|}. \tag{2}$$

The dislocation (edge or screw) gliding in that plane produces a plastic strain-rate proportional to its Schmid tensor $\mathbf{S}^g$, according to the Orowan equation

$$\dot{\varepsilon}_{ij}^g = \rho b v^g S_{ij}^g \tag{3}$$

with $S_{ij}^g = \frac{1}{2}\left(n_i^g \hat{b}_j + n_j^g \hat{b}_i\right)$, where $\hat{\mathbf{b}}$ is the unit vector parallel to $\mathbf{b}$, ρ is the density of mobile dislocations and v^g is their glide velocity. The inclination θ between the dislocation plane and the glide plane (Figure 4) can be calculated from $\cos\theta = \mathbf{n}^g \cdot \mathbf{n}$. For non-zero values of θ, climb must be involved. The kinematics of the climb of an edge dislocation is a little more complicated as diffusion may not produce an isochoric strain (see Lebensohn et al., 2010; Yuan et al., 2018). However, considering geological time scales, we assume that the density of point defects that affect climb achieves equilibrium concentrations (i.e., constant with time) at a given temperature. Thus, no volume change is expected due to climb. The strain-rate tensor produced by climb is proportional to the "climb Schmid tensor" $\mathbf{S}^c$ (index.^{c} stands for climb)

$$\dot{\varepsilon}_{ij}^c = \rho b v^c S_{ij}^c \tag{4}$$

where v^c is the climb rate of the segment and $\mathbf{S}^c$ is given by $S_{ij}^c = \hat{b}_i \hat{b}_j - \frac{1}{3}\hat{b}_k \hat{b}_k \delta_{ij}$. As indicated in Tables S1 and S2 in Supporting Information S1, several dislocation segments and movement planes have been identified in the two grains investigated. Grain deformation can be investigated by summing-up the contributions of glide and/or climb of one or more dislocation segments, and the number of the associated independent deformation systems can be computed as explained in Cotton & Kaufman (1991) and Castelnau et al. (2020) for any crystal symmetry.

2.5. Estimation of the Local Loading Conditions

Here we attempt to infer the local stress that acted in situ on the investigated grain to produce the observed dislocation microstructure. We assume a power law constitutive relation for glide and for climb to estimate the dislocation velocity for glide and climb. These velocities, which depend on the local stress, are linked together by the angle θ shown in Figure 4.

2.5.1. Glide

We start with the Orowan equation (Equation 3), written for a specific slip system and consider a standard power-law (Morales et al., 2011) to describe the shear-rate at the slip system scale:

$$\dot{\gamma} = \dot{\gamma}_0 \left|\frac{\tau}{\tau_0}\right|^{n_g - 1} \frac{\tau}{\tau_0} \tag{5}$$

where $\dot{\gamma}_0$ is a reference strain-rate, τ_0 is the corresponding reference stress, n_g gives the stress sensitivity for glide, and τ is the shear stress resolved on the glide plane given by:

$$\tau = n_i^g \hat{b}_j \sigma'_{ij} \tag{6}$$

The dislocation glide velocity is thus given by:

$$v_g = \frac{\dot{\gamma}_0}{\rho b} \left|\frac{\tau}{\tau_0}\right|^{n_g - 1} \frac{\tau}{\tau_0} \tag{7}$$

2.5.2. Climb

Here we use the Orowan equation (Equation 4) adapted to climb, following Lebensohn et al. (2010). As for glide, we consider a standard power-law to describe the longitudinal strain-rate:

$$\dot{\varepsilon} = \dot{\gamma}_0 \left|\frac{\sigma'}{\sigma_0}\right|^{n_c - 1} \frac{\sigma'}{\sigma_0} \tag{8}$$

where $\dot{\gamma}_0$ is a reference strain-rate (which can be taken as the same as for glide), σ_0 is the corresponding reference stress, n_c gives the stress sensitivity for climb, and σ' is the deviatoric stress given by:
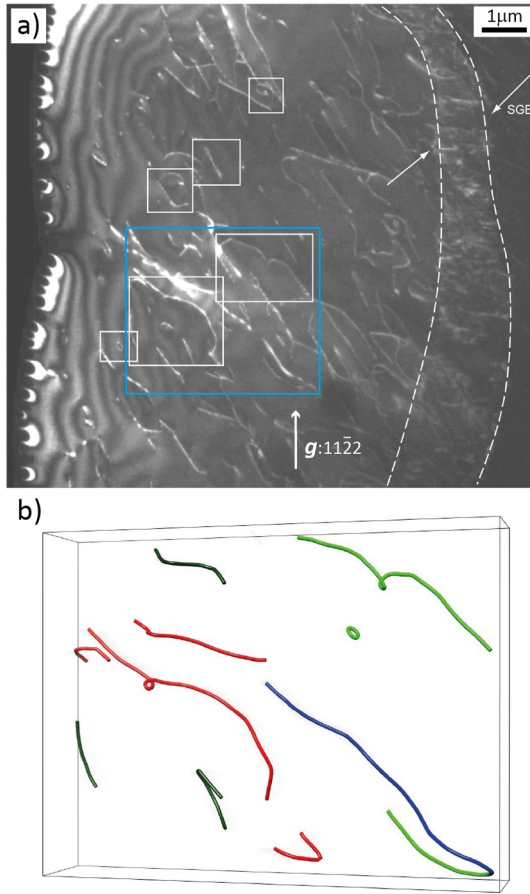
Figure 5. Global microstructure of the Main Central Thrust specimen: (a) Micrograph in weak-beam dark-field condition obtained with the $11\bar{2}2$ diffraction vector (the white rectangles are analyzed in detail in this study), where one subgrain boundary (SGB) can be observed on the right (arrows, the subgrain wall between the dashed lines is visible during tit-experiments). (b) Dislocation Electron Tomography 3D model of the region outlined in blue in (a), viewed along the same direction (projection angle $-15°$) (see also Supplementary Movie S1). The color code represents the Burgers vector: green stands for $1/3\left[1\bar{2}10\right]$, dark green stands for $1/3\left[1\bar{2}13\right]$, red stands for $1/3\left[11\bar{2}0\right]$ and blue stands for $1/3\left[2\bar{1}\bar{1}0\right]$.

$$\sigma' = \hat{b}_i\hat{b}_j\sigma'_{ij} \tag{9}$$

The dislocation climb velocity is thus given by:

$$v_c = \frac{\dot{\gamma}_0}{\rho b}\left|\frac{\sigma'}{\sigma_0}\right|^{n_c-1}\frac{\sigma'}{\sigma_0}. \tag{10}$$

2.5.3. Estimation of the Local Stress

The velocities v_c and v_g are related by the angle θ between the normal to the plane of movement and the normal to the glide plane. This can be expressed as

$$\left(v_g\hat{\mathbf{b}} + v_c\mathbf{n}^g\right).\,\mathbf{n} = 0 \tag{11}$$

where $\cos\theta = \mathbf{n}^g.\,\mathbf{n}$. To find a stress state compatible with the observed dislocation structure, we must solve for a system of nonlinear equations formed by one condition (Equation 11) for each observed dislocation segment. We adopt a minimization procedure in order to find the stress tensor that best matches the observations. We construct the following objective function

$$\sum_s l_s^k\left(\theta_s^{mod} - \theta_s^{obs}\right)^2 \tag{12}$$

where θ^{mod} is the θ angle computed from the above equations and θ^{obs} is the observed angle. The difference in θ angles is weighted by the dislocation length l to the power k in order to force a better match for longer dislocation segments (here, we used a value $k = 4$). The objective function is the sum over all observed dislocation segments s, minimized by the Nelder–Mead method.

3. Results

The dislocation microstructures of the MCT and MT specimens are comparable. Dislocation densities are 3×10^{12} m^{-2} and 4×10^{12} m^{-2} respectively (with densities measured directly from the reconstructed volumes). Subgrain boundaries due to recovery are observed in both specimens (Figures 5a and 6a).

In this section, the quantitative analysis of the microstructure is described, followed by a detailed characterization of slip systems, and then climb systems for each specimen. From these analyses, Schmid tensors and associated equivalent strain and stress tensors of each specimen are estimated.

3.1. Quantitative Analysis of the Microstructure

The characterization of dislocation glide and/or climb relies on determination of the plane of movement of the dislocation, which can only be achieved for curved dislocations. In this study, however, we have sought to take into account the contribution of rectilinear dislocations to the microstructure. Lattice friction is high in quartz under the deformation conditions of our specimens (Doukhan & Trépied, 1985). Consequently, it is highly likely that rectilinear dislocations are in glide configurations. Following the characterization of direction lines of rectilinear dislocations with known Burgers vectors, it is possible to infer their glide planes (provided that they are not pure screw in character). In order to optimize the quantification of the dislocation glide and climb contributions, we have only considered the dislocations whose Burgers vectors could be determined unambiguously, keeping in mind that indexing of Burgers vectors has previously been optimized (see Section 2.3). However, DET
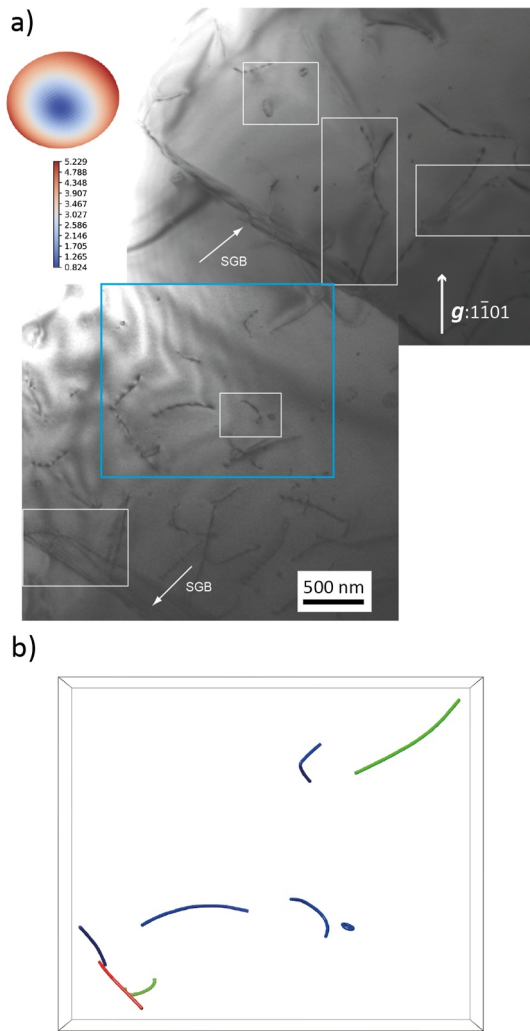
Figure 6. Global microstructure of the Moine Thrust specimen: (a) Micrograph in bright-field condition obtained with the $1\bar{1}01$ diffraction vector (the white rectangles are analyzed in detail in this study) where two subgrain boundaries (SGB) can be observed (indicated by white arrows). In the top left corner is the stress ellipsoid inferred from the present analysis (see discussion, Figure 15 and Supplementary Movie S8). (b) Dislocation Electron Tomography 3D model of the region outlined in blue in (a), viewed along the same direction (projection angle 0°) (see also Supplementary Movie S2). The color code represents the Burgers vector: green stands for $1/3\left[1\bar{2}10\right]$, red stands for $1/3\left[11\bar{2}0\right]$ and blue stands for $1/3\left[2\bar{1}\bar{1}0\right]$.

has been conducted for each specimen with only one diffraction vector which does not allow identification of all dislocation segments. More precisely, the DET study of the MCT specimen has been conducted with the $11\bar{2}2$ diffraction vector, where all dislocations ($\langle a\rangle$, [c] and $\langle c+a\rangle$) are in contrast except $\boldsymbol{c}+\boldsymbol{a}_3$ dislocations. Our DET study of the MT specimen has been conducted with the $1\bar{1}01$ diffraction vector where all dislocations are in contrast except $\boldsymbol{a}_3$, $\boldsymbol{c}+\boldsymbol{a}_2$ and $\boldsymbol{c}-\boldsymbol{a}_1$.

3.2. Glide

3.2.1. MCT Specimen

In this specimen, we found evidence of $\langle a\rangle$ and $\langle c+a\rangle$ glide in prismatic $\{1\bar{1}00\}$ planes, and also of $\langle a\rangle$ glide in pyramidal $\{1\bar{1}01\}$ planes and in a $(1\bar{1}02)$ pyramidal plane.

An example of tomographic reconstruction of a typical domain is shown in Figure 7. The Burgers vector indexing shows the presence of dislocations with $\frac{1}{3}[1\bar{2}10]$ (or $\boldsymbol{a}_2$) and $\frac{1}{3}[1\bar{2}13]$ (or $\boldsymbol{c}-\boldsymbol{a}_2$) Burgers vectors, drawn in light and dark green, respectively. The reconstructed dislocation volumes can be tilted to view the planes containing these dislocations edge-on. Figures 7a–7c, show an $\boldsymbol{a}_2$ dislocation lying near the prismatic $(10\bar{1}0)$ plane. This demonstrates activation of the $\frac{1}{3}[1\bar{2}10](10\bar{1}0)$ slip system. A slightly more complex configuration is detailed in Figures 7d–7f. Part of this dislocation is in the $(10\bar{1}0)$ glide plane. Moreover, a collinear interaction (Madec et al., 2003; Mussi et al., 2015) with an $\boldsymbol{a}_2$ sessile dislocation loop can be clearly identified. The plane of this loop is edge-on for a projection angle (A projection angle is the angle between the normal of the specimen thin foil and the direction of the electron beam for a particular tilt angle) of −38° (Figure 7f). The 3D geometry of this dislocation is due to this interaction. From Figures 7g–7i, we also characterize the $\frac{1}{3}[1\bar{2}13](10\bar{1}0)$ slip system.

3.2.2. MT Specimen

The MT specimen also shows dislocations in glide configurations. We found evidence for glide of $\langle a\rangle$, [c] and $\langle c+a\rangle$ dislocations. In this specimen, no prismatic glide has been observed for $\langle a\rangle$ and $\langle c+a\rangle$ dislocations; only [c] dislocations in $(1\bar{1}00)$ and $(\bar{2}110)$ glide planes have been characterized. $\langle a\rangle$ dislocations appear to glide predominantly in $\{1\bar{1}01\}$ pyramidal planes. We have also noted evidence for $\langle a\rangle$ glide in $\{1\bar{1}02\}$ and $\{2\bar{2}01\}$, and $\langle c+a\rangle$ glide in $\{\bar{1}01\bar{1}\}$, $\{11\bar{2}\bar{1}\}$, $\{11\bar{2}2\}$ and $\{21\bar{3}\bar{1}\}$. Glide in $\{1\bar{1}01\}$ represents approximately 3/7 of all dislocation glide evaluated in this specimen. An example of a slip system characterization is shown in Figures 8a–8d. The pyramidal $(11\bar{2}\bar{1})$ plane is edge-on with a projection angle of 14°. The direction of the trace of this plane corresponds to the direction of the dislocation line with a projection that is rectilinear, as its movement plane is edge-on (Figure 8b). The $\frac{1}{3}[2\bar{1}\bar{1}3](11\bar{2}\bar{1})$ slip system has been identified given that the Burgers vector of this dislocation is $\boldsymbol{c}+\boldsymbol{a}_1$. We have also identified the $[0001](2\bar{1}\bar{1}0)$ slip system (Figures 8e–8h).

3.3. Climb

3.3.1. MCT Specimen

A significant proportion of the dislocation population cannot be interpreted as resulting from glide (i.e., lying in a plane which contains the Burgers vector). For instance, Figures 9a–9c show a $\frac{1}{3}[11\bar{2}0]$ dislocation ($\boldsymbol{a}_3$) in a $(11\bar{2}0)$ plane. This corresponds to a prismatic loop in pure climb configuration. A complex 3D dislocation
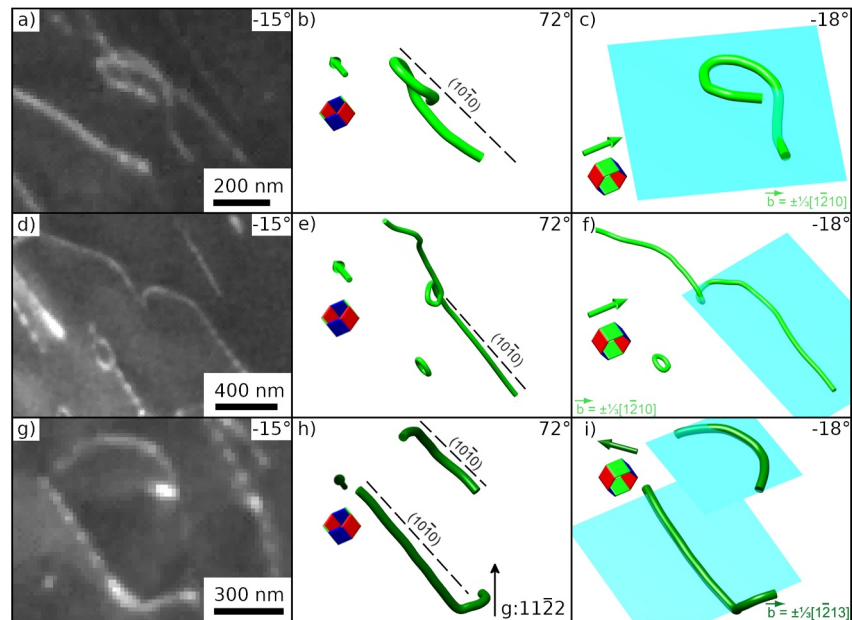
Figure 7. Slip system characterizations by dislocation electron tomography for the Main Central Thrust specimen, obtained with the $11\bar{2}2$ diffraction vector: (a) Raw weak-beam dark-field (WBDF) micrograph of a $\boldsymbol{a}_2$ dislocation observed along a projection angle of $-15°$; (b) reconstructed volume of this dislocation (colored in green) for a projection angle of $72°$ where the prismatic $(10\bar{1}0)$ plane is edge-on; (c) same reconstructed dislocation with a projected angle of $-18°$; (d) raw WBDF micrograph of two $\boldsymbol{a}_2$ dislocations (a dislocation loop and a complex 3D dislocation) observed along a projection angle of $-15°$; (e) reconstructed volume of these dislocations for a projection angle of $72°$; (f) same reconstructed dislocations with a projected angle of $-18°$; (g) raw WBDF micrograph of 3D $\boldsymbol{c} - \boldsymbol{a}_2$ dislocations observed along a projection angle of $-15°$; (h) reconstructed volume of these dislocations (colored in dark green) for a projection angle of $72°$; (i) same reconstructed dislocations with a projected angle of $-18°$. The $\frac{1}{3}[\bar{1}2\bar{1}0](10\bar{1}0)$ and $\frac{1}{3}[\bar{1}\bar{2}13](10\bar{1}0)$ slip systems have been characterized in this figure. The hexagonal prism is a visual aid to the orientation of the quartz crystal lattice (For interpretation of the references to color in this caption, the reader is referred to the web version of this article).

(Figures 9d–9f) has been analyzed where one of its segments is practically in pure climb configuration (Figure 9f) and three other segments are neither in pure climb, nor in pure glide configurations. In other words, the Burgers vector of this dislocation makes an angle with the plane containing each segment under consideration with values between 0 and 90° (such as in Figure 4). These configurations are characterized as mixed climb, as kinematically described in Section 2.4. We also note that this dislocation shows collinear climb interaction with a prismatic loop. Figures 9g–9i show an example of mixed climb, which involves a $\boldsymbol{c} - \boldsymbol{a}_2$ dislocation. Of all dislocations analyzed in the MCT specimen, approximately 3/5 are of mixed climb character (considering the lengths of the dislocation segments).

3.3.2. MT Specimen

We find the same results for the MT specimen as for the MCT specimen, with a significant proportion (around half) of dislocations in mixed climb configurations (Figures 10d–10f and 10g–10i). An example of a small dislocation loop in a pure climb configuration has also been found (Figures 10a–10c).

3.4. Strain Analysis From Electron Tomography Data

The plastic strain inferred for the motion of each dislocation segment has been calculated based on the relations provided in Section 2.4. We have considered, for each specimen, (a) the segments that correspond to pure glide ($\theta = 0$) only, (b) the segments in pure climb configurations ($\theta = 90°$) only, (c) all glide components of the segments (i.e., including pure glide segments and the glide contribution of segments in mixed climb configurations), and (d) all climb components (i.e., pure climb segments and the climb contributions of segments in mixed climb configurations). In all cases except in the case of pure climb, the set of available dislocations is sufficient to provide five independent strain components at the grain scale. Thus, the observed dislocation microstructure can
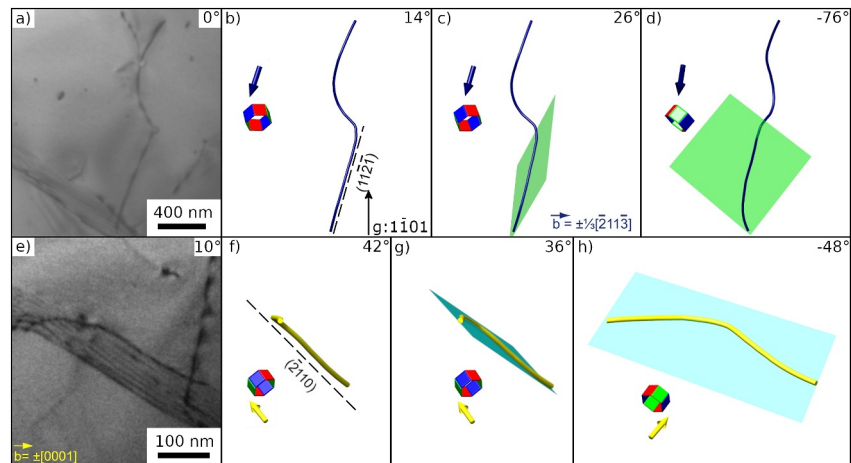
Figure 8. Slip system characterizations revealed by dislocation electron tomography, obtained with the $1\bar{1}01$ diffraction vector, in the Moine Thrust specimen: (a) Raw bright-field micrograph of a $\boldsymbol{c} + \boldsymbol{a}_1$ dislocation observed along a projection angle of 0°, intersecting two fine-scale fluid inclusions; (b) reconstructed volume of this dislocation (colored in dark blue) for a projection angle of 14° where the pyramidal $(11\bar{2}\bar{1})$ plane is nearly edge-on; (c) same reconstructed dislocation with a projected angle of 26° (green plane shows the habit plane of the dislocation segment); (d) same reconstruction with a projected angle of −76° (the normal to the pyramidal plane appears edge-on in this image); (e) raw bright-field micrograph of a [c] dislocation observed along a projection angle of 10°; (f) reconstructed volume of this dislocation (colored in yellow) for a projection angle of 42° where the prismatic $(\bar{2}110)$ plane is edge-on; (g) same reconstructed dislocations with a projected angle of 36°; (h) same reconstruction with a projected angle of −48° (the normal to the prismatic plane appears edge-on in this image). The $\frac{1}{3}[\bar{2}11\bar{3}](11\bar{2}\bar{1})$ and $[0001](\bar{2}110)$ slip systems have been characterized in this Figure. The hexagonal prism is a visual aid to the orientation of the quartz crystal lattice (For interpretation of the references to color in this caption, the reader is referred to the web version of this article).

accommodate any deformation. The Schmid tensors, either for glide or for climb, are full matrices (presented in the supplements) in which no specific component dominates. The associated equivalent Schmid tensors, $\overline{S}^g_{eq} = \left(\overline{S}^g_{ii}\right)^{\frac{1}{2}}$ for all glide contributions and $\overline{S}^c_{eq} = \left(\overline{S}^c_{ii}\right)^{\frac{1}{2}}$ for all climb contributions, have similar values, about 0.2 for MT for both glide and climb. Somewhat smaller values are obtained for glide (∼0.1) than for climb (∼0.4) for the MCT specimen.

4. Discussion

4.1. Slip Systems

In our specimens, dislocations observed are mostly of the $\langle a \rangle$ and $\langle c + a \rangle$ types with only few [c] dislocations observed in the MT specimen. Active slip systems in quartz have been constrained by many experimental studies (Baëta & Ashbee, 1969; Hobbs, 1968; Morrison-Smith et al., 1976) and their activities have been shown to depend strongly on temperature and stress. Below 700°C, $\langle a \rangle$ basal glide dominates. Above 700°C, glide becomes progressively more active in pyramidal ($\{1\bar{1}0n\}$ with n = 1, 2, 3), and then on prismatic planes. Above 750°C, $\langle c + a \rangle$ dislocations are activated which glide in $\{1\bar{1}01\}$ and $\{11\bar{2}n\}$ families of planes with n = 1, 2 and then [c] glide on prismatic planes. Under geological conditions of strain-rate and deviatoric stress, the same sequence is assumed to be valid with the activation of [c] glide starting at 600–650°C (Mainprice et al., 1986; Okudaira et al., 1995). Mainprice et al. (1986) also point out that the activation of [c] glide is favored by wet conditions, which is the case in our specimens. Our observations are thus consistent with this transition sequence where $\langle a \rangle$ basal glide is not active, [c] glide is of marginal importance, and $\langle a \rangle$ slip occurs predominantly on pyramidal and prismatic planes at the high temperature, low strain rate conditions of these shear zones, in which hydrogen defects have access to dislocation cores. However, this study has led to an additional and remarkable observation: activation of $\langle c + a \rangle$ glide is widespread in the $\{10\bar{1}0\}$, $\{10\bar{1}1\}$, $\{11\bar{2}n\}$ (n = 1, 2) and even $\{21\bar{3}1\}$ (not previously reported) planes. Glide along $\langle c + a \rangle$ is generally expected at high temperatures (Baëta & Ashbee, 1969). However, while $\langle c + a \rangle$ glide is reported in the literature, it has been the subject of far fewer detailed observational studies than $\langle a \rangle$ and [c] glide, particularly in natural specimens. We had previously observed $\langle c + a \rangle$ dislocations
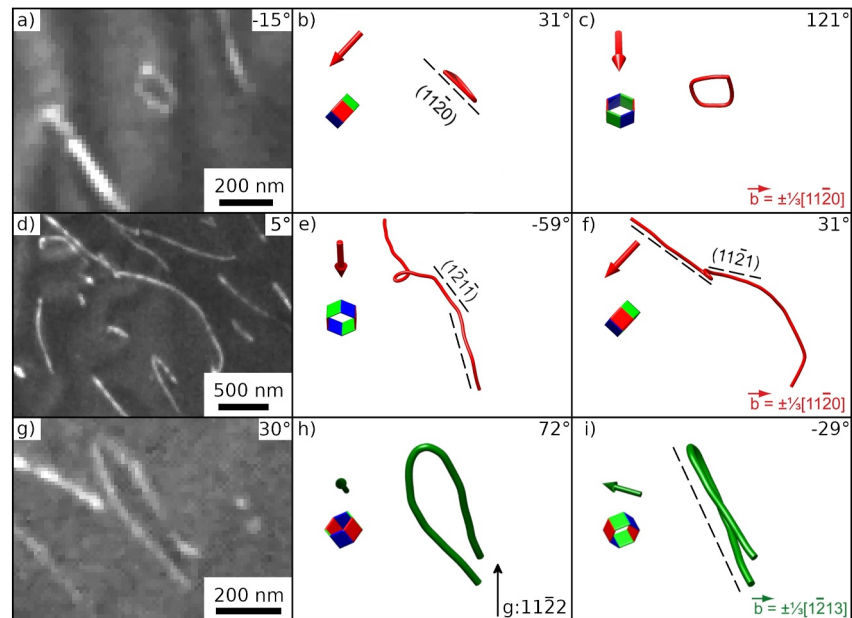
Figure 9. Climb characterizations revealed by dislocation electron tomography, obtained with the $11\bar{2}2$ diffraction vector, for the Main Central Thrust specimen: (a) Raw weak-beam dark-field (WBDF) micrograph of a $\boldsymbol{a}_3$ dislocation observed along a projection angle of $-15°$; (b) reconstructed volume of this dislocation (colored in red) for a projection angle of $31°$ where the prismatic $(11\bar{2}0)$ plane is edge-on; (c) same reconstructed dislocation with a projected angle of $121°$; (d) raw WBDF micrograph of another geometrically complex $\boldsymbol{a}_3$ dislocation observed along a projection angle of $5°$; (e) reconstructed volume of this dislocation for a projection angle of $-59°$ where the pyramidal $(1\bar{2}1\bar{1})$ plane is edge-on; (f) the same dislocation with a projected angle of $31°$ where the pyramidal $(11\bar{2}1)$ plane is edge-on; (g) raw WBDF micrograph of a $\boldsymbol{c} - \boldsymbol{a}_2$ dislocation observed along a projection angle of $30°$; (h) the reconstructed volume of this dislocation (colored in dark green) for a projection angle of $72°$; (i) the same reconstructed dislocation with a projected angle of $-29°$ for which its plane is edge-on. The $\frac{1}{3}[11\bar{2}0](11\bar{2}0)$ pure climb system and the $\frac{1}{3}[11\bar{2}0](11\bar{2}1)$ and $\frac{1}{3}[11\bar{2}0](1\bar{2}1\bar{1})$ mixed climb systems have been characterized in this figure. The hexagonal prism is a visual aid to the orientation of the quartz crystal lattice (For interpretation of the references to color in this figure legend, the reader is referred to the web version of this article).

in a Bohemian granulite (Mussi, Gallet et al., 2021). Yet in many studies that depend on extracting geometrically necessary dislocation densities from EBSD measurements (Wallis et al., 2019) or modeling crystal preferred orientations (e.g., Keller & Stipp, 2011; Morales et al., 2011), $\langle c + a \rangle$ glide has been neglected. Determinations of geometrically "necessary" dislocation densities from measured lattice distortions rely on knowing the displacement vectors of the individual dislocations that are generated and remain within quartz grains. General strains can fictively be explained by assuming activation of dislocation systems with other Burgers vectors (without $\langle c + a \rangle$ glide), but such suppositions are contrary to the results of this study.

4.2. Mixed Climb

The most important observation of this study is the significant activation of climb over a wide range of middle to deep crustal temperatures and tectonic strain rates. Besides some evidence for dislocations in pure climb configuration, we found pervasive evidence of mixed climb (Carrez et al., 2024) of $\langle a \rangle$ and $\langle c + a \rangle$ dislocations. The long-standing problem of accommodating any arbitrary strain can be solved for quartz either by activation of $\langle c + a \rangle$ glide, or climb. We show here that both operate together with $\langle c + a \rangle$ dislocations that exhibit mixed climb geometries. Moreover, we show that the contribution of glide produced by the observed microstructures is sufficient to accommodate any arbitrary strain. Hence, activation of climb is not necessary to provide additional strain components. However, we show that climb provides an additional contribution to strain comparable to that of glide.

Activation of dislocation climb in quartz has been recognized for many decades (White, 1977), especially under wet conditions when internal water contents exceed the solubility limit of water-related defects (Cordier & Doukhan, 1989; Kirby & McCormick, 1979; McLaren et al., 1989). Climb is generally inferred by the absence of
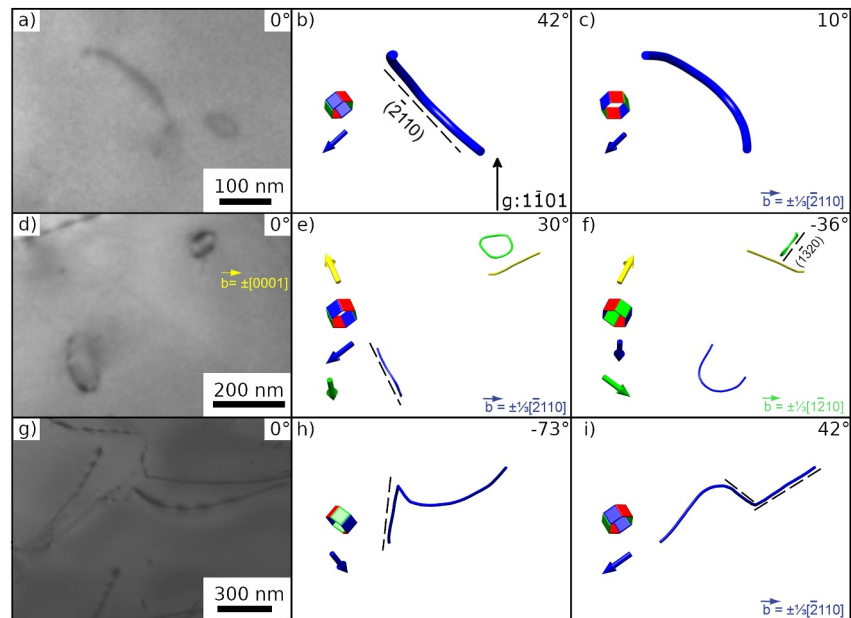
Figure 10. Characterizations of dislocation climb revealed by dislocation electron tomography, obtained with the $1\bar{1}01$ diffraction vector, for the Moine Thrust specimen: (a) Raw bright-field micrograph of a $\boldsymbol{a}_1$ dislocation observed along a projection angle of 0°; (b) reconstructed volume of this dislocation (colored in blue) for a projection angle of 42° for which the prismatic $(\bar{2}110)$ plane is edge-on; (c) same reconstructed dislocation with a projected angle of 10°; (d) raw bright-field micrograph of $\boldsymbol{a}_1$, $\boldsymbol{a}_2$ and $\boldsymbol{c}$ dislocations observed along a projection angle of 0°; (e) reconstructed volume of these dislocations (colored in blue, green and yellow respectively) for a projection angle of 30° where the habit plane of the $\boldsymbol{a}_1$ dislocation loop is edge-on; (f) same reconstructed dislocations with a projected angle of −36° where the prismatic $(1\bar{3}20)$ plane is edge-on (corresponding to the habit plane of the $\boldsymbol{a}_2$ dislocation loop); (g) raw bright-field micrograph of a $\boldsymbol{c} - \boldsymbol{a}_2$ complex dislocation observed along a projection angle of 0°; (h) reconstructed volume of this dislocation for a projection angle of −73° where the habit plane of a part of this dislocation is edge-on; (i) same reconstructed dislocation with a projection angle of 42° where the last two parts of this dislocation are edge-on. The $\frac{1}{3}[\bar{2}110](\bar{2}110)$ pure climb and the $\frac{1}{3}[1\bar{2}10](1\bar{3}20)$ mixed climb systems are characterized in this figure. The hexagonal prism is a visual aid to the orientation of the quartz crystal lattice (For interpretation of the references to color in this caption, the reader is referred to the web version of this article).

apparent lattice friction (curved and entangled dislocations) and by the presence of subgrain boundaries (Baëta & Ashbee, 1973; Ball & Glover, 1979), as found in our two specimens. Under all conditions that climb is significant, it is considered an important recovery mechanism (Tullis & Yund, 1989). Indeed, dislocation creep is usually described within the framework of Weertman (1968) creep where the strain is produced by dislocation glide whose resulting hardening is counterbalanced by a recovery mechanism, generally involving dislocation climb. It is implicit that dislocation glide produces most of the strain, while climb produces little strain but controls the strain-rate. This means that the glide velocity is supposed to be much greater (several orders of magnitude greater) than the climb velocity. On this basis, Boioli et al. (2015) modeled creep in olivine above 1400 K with a glide velocity more than a thousand times faster than the climb velocity under low stress.

Our observation of pervasive mixed glide and climb with movement planes taking any orientation between pure glide and pure climb in quartz mylonites of the MCT and MT (Figure 11) suggests that velocities of dislocation glide and climb were comparable. In this case, climb and glide are both strain-producing mechanisms. Deformation microstructures of γ-TiAl alloys deformed at 770–790°C have led to the same observation, with a transition in the temperature/strain-rate domain where climb can reach the velocity of glide (Couret, 2010; Galy et al., 2023; Malaplate et al., 2004; Voisin et al., 2016). Preferential mixed climb has also been characterized in minerals such as olivine (Mussi et al., 2017) and MgO (Mussi, Carrez et al., 2021). Such mixed climb motions may be difficult to recognize without the characterization of both Burgers vectors and dislocation lines. However, we may well wonder whether this mechanism can be inferred from less detailed observations.

Early studies of deformation lamellae in quartz deformed in laboratory experiments (Blacic, 1975; Christie et al., 1964; Hobbs, 1968; Trepmann & Stöckhert, 2013; Tullis et al., 1973) and under natural, crustal conditions
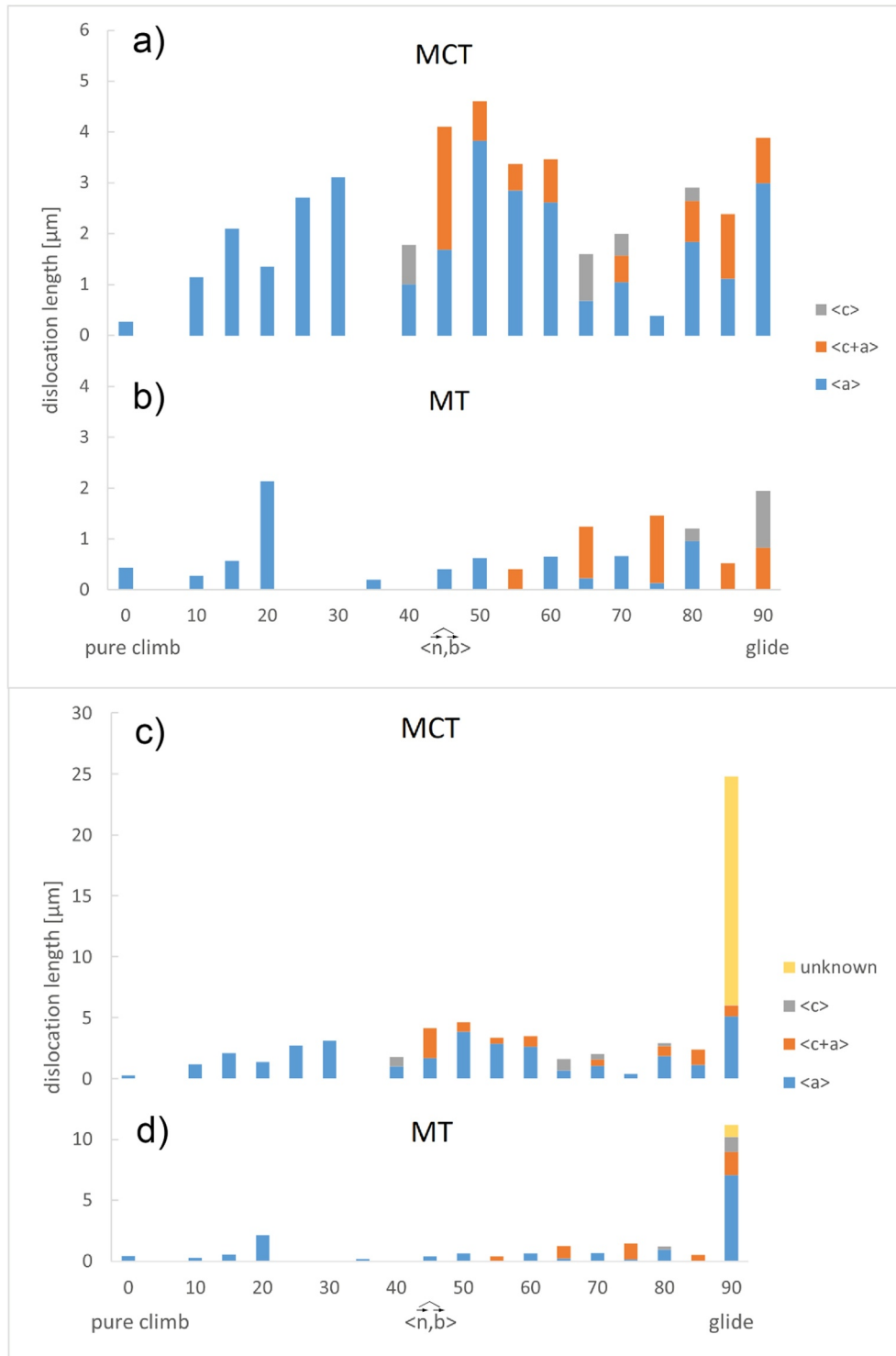
Figure 11. Histograms quantifying the climb contribution in quartz of [c], $\langle c + a \rangle$, and $\langle a \rangle$ dislocations: (a) Histogram of the evolution of the angle between Burgers vectors and normal vectors to habit planes $\widehat{(n, b)}$ normalized for dislocation segment lengths for the Main Central Thrust (MCT) specimen; (b) histogram for the Moine Thrust (MT) specimen; (c) MCT specimen: histogram where the lengths of straight-line dislocation segments are included, considering these segments are in a glide configuration; (d) MT specimen: histogram where the lengths of straight-line dislocation segments are included. From these histograms, more than 50% of the dislocation length is found in climb configurations.

(e.g., McLaren & Hobbs, 1972; Sylvester, 1969; Trepmann & Stöckhert, 2003) were taken as evidence of slip on basal and prismatic planes. However, these planar optical features commonly occur at angles of up to 15–30° from rational crystallographic planes perpendicular and parallel to c (Christie & Ardell, 1974; Heard & Carter, 1968; Hobbs, 1968; Tullis et al., 1973). Characterized optically by their anomalous refractive index, deformation lamellae observed by TEM were found to consist of lamellar zones of highly tangled dislocations rather than simple arrays of free dislocations in their anticipated slip planes (Christie & Ardell, 1976). Detailed TEM diffraction analysis of the tangled dislocations within these lamellae has not been possible. Nevertheless, Vernooij (2005) posed the hypothesis that orientations of deformation lamellae, like slip bands, reveal directions of dislocation motion, and therefore give relative velocities of glide within basal and prism planes, and climb out of these planes. Heard and Carter (1968) showed that non-basal deformation lamellae are favored by high temperature (and low strain rate), as may be expected for higher climb velocities at higher temperatures. Misorientations of deformation lamellae may therefore result from some climb accompanying glide. Still, the tangled nature of dislocations within lamellar regions of early experiments indicates that climb was insufficient for significant recovery.

Much higher rates of dislocation climb and recovery are evident from the microstructures of MCT and MT quartzites and the DET analyses of this study. Compiling our results for these natural quartz shear zone specimens, Table 1 summarizes length-weighted proportions of dislocations found in glide, pure climb, and mixed glide-climb orientations.

Glide-producing dislocation lines constitute *ca*. 38% of the total in the MCT specimen and approximately 50% for the MT specimen. More than half of the total dislocation line lengths analyzed involve some climb (pure or mixed) component in both specimens. Considering the length of each dislocation segment and measuring the angle between Burgers vector and normal vector to each plane of motion $\widehat{(n, b)}$, histograms can be plotted for all dislocation segments to quantify the climb contribution for each kind of Burgers vector. The $\widehat{(n, b)}$ angle ranges from 0° for pure climb to 90° for glide configurations (see Figure 11). Figures 11a and 11c describe the climb distribution of the MCT specimen without and with rectilinear dislocation segments respectively. Similarly Figures 11b and 11d show the climb distributions for MT specimens without and with rectilinear dislocation segments, respectively. These histograms show no significant difference between dislocation microstructures in specimens MCT and MT. $\langle a \rangle$ dislocations are found most often in climb or mixed climb orientations.

Our calculations (Section 3.4) for both MCT and MT specimens indicate that plastic strains produced by climb are of the same order of magnitude (possibly larger for the MCT specimen) as produced by glide. MCT and MT specimens were deformed extensively by dislocation creep in the presence of water. Abundant fluid inclusions that intersect with dislocations suggest that dislocation mobilities in these specimens have probably been facilitated by access to hydrous defects within dislocation cores that increase rates of dislocation glide and/or climb (Cordier & Doukhan, 1989; Kirby & McCormick, 1979; McLaren et al., 1989). However, our characterizations do not allow us to draw any further conclusions about the potential role of hydrous defects on climb, including mixed climb.

The fact that plastic strains produced by climb and glide are of the same order of magnitude is an important observation, as it bears on interpretations of CPO of rock deformed by dislocation creep. In recent studies, deformation is taken to be due to glide on the $\langle a \rangle$ basal system, then $\langle a \rangle$ prismatic/pyramidal slip, and then [c] prismatic slip with increasing temperature (Keller & Stipp, 2011; Morales et al., 2011, 2014; Okudaira et al., 1995; Tokle et al., 2019). Changes in proportions of different slip systems activated at different temperatures and strain rates are presumably reflected in c-axis fabrics of quartz mylonites, with an opening angle about the normal to foliation for pure shear that constitutes a balance between slip systems that rotate c-axes toward the maximum compressive stress (normal to foliation) and those that rotate c-axes toward foliation. Conceptual and numerical models of CPO development (e.g., Lister & Hobbs, 1980; Tullis et al., 1973; Wenk et al., 1989, 2019) are based on varying proportions of dislocation glide on $\langle a \rangle$ basal, $\langle a \rangle$ prism, $\langle a \rangle$ pyramidal, [c] prism, and $\langle c + a \rangle$ pyramidal systems, but we know of no models that incorporate $\langle c + a \rangle$ prism glide or climb as a strain mechanism. Revisions to our interpretation of CPO will need to include the addition of slip with displacement vector $\langle c + a \rangle$ on prism and other planes. Kinematically, adding $\langle c + a \rangle$ glide will alter the proportions of $\langle a \rangle$ and [c] glide. Moreover, if only glide is considered, we will miss a significant fraction of the strain accomplished during dislocation creep.

Table 1

Proportion of Dislocation Segments in Glide, Pure Climb and Mixed Climb Configuration for Each Specimen, Depending on Whether or Not Straight Segments Are Included in the Counting

		MCT specimen		MT specimen	
Without straight dislocation segments	% Glide	9		16	
	% Pure climb	1	91	3	84
	% Mixed climb	90		81	
With straight dislocation segments	% Glide	38		51	
	% Pure climb	1	62	2	49
	% Mixed climb	61		47	

Deformation thermometers such as the quartz c-axis fabric opening angle thermometers of Kruhl (1998) and Faleiros et al. (2016) rely on fabric observations and determined temperatures of deformation. They do not explicitly take into account the separate potential influences of different slip systems or the balance of glide and climb on fabric development. However, the interpretation of these empirically based thermometers will depend on activation of slip systems at varying temperature, strain rate and action of hydrous defects. Relations between glide-induced CPO and total strain will further depend on how much strain is accomplished by glide and by climb.

4.3. Inferring Stress Loading

Sylvester (1969) suggested that deviations of deformation lamellae orientations from rationale crystallographic planes tend toward planes of high shear stress, potentially offering a tool to reconstruct internal stresses. Here, we explore this hypothesis further. To do this, we represent on Figure 12 the different systems (glide or climb) on a stereographic projection for quartz where positive vertical [0001] is shown vertical (upper hemisphere). Figure 12a summarizes our observations for the different types of dislocations, color-coding the contribution of climb. From this stereographic projection (Figure 12b), we can see that the orientation of the grain analyzed in the MCT specimen strongly enhances activation of the $1/3[1\bar{2}10](10\bar{1}0)$ glide system. As a result, there is little climb of $1/3[1\bar{2}10]$ dislocations. In contrast, glide of $1/3[11\bar{2}0]$ dislocations is less favorable (Figure 12c) increasing the tendency to climb.

In Figure 12d, we extract the glide components of the mixed climb planes of $1/3[11\bar{2}0]$ dislocations into the pure climbing plane normal (along the $[11\bar{2}0]$ direction), but also on the glide plane normal depicted in Figure 4.

This analysis reveals the strain contributions of two easy slip systems: $1/3[11\bar{2}0](\bar{1}100)$, $1/3[11\bar{2}0](\bar{1}101)$ and, to a lesser extent, of $1/3[11\bar{2}0]$ on $(\bar{1}10n)$ and other unexpected planes. Such evidence of glide in planes that have not been reported for quartz raises questions. Dislocation motion in these planes does not correspond to pure glide, but is associated with mixed climb. This observation is in line with interpretations made of mixed climb in TiAl alloys. According to Malaplate et al. (2004), dislocation motion in mixed climb planes may be facilitated by reduced lattice friction during pure glide (probably linked to specific dislocation core structures). We hypothesize that activation of mixed glide and climb may allow activation of glide on additional planes. This hypothesis, based as it is on preliminary observations, requires further observational and theoretical investigation.

We apply the method described in Section 2.5.3 to learn whether the stress state that acted in situ can be inferred. Several minimization attempts have been carried out, and slightly better results have been obtained when allowing different slip resistances τ_0 for dislocations with $\langle a \rangle$, $\langle c + a \rangle$, and $[c]$ Burgers vectors. Results (Figure 13 for MT) show a good match between the observed and computed θ values. In the minimization procedure, we needed to optimize not only for stress state but also the rheological parameters. Best results are obtained for a nearly linear response to stress for both glide and climb ($n_g \approx n_c \approx 1$) and slip resistances for $\langle c + a \rangle$ and $[c]$ dislocations just half the slip resistance for $\langle a \rangle$ dislocations.

The stress state obtained in this way for the quartz grain MT at the time of deformation indicates that the larger normal stress (promoting climb) acted on planes perpendicular to directions close to $\langle c + a \rangle$ and that the maximum shear stress (promoting glide) appeared to have been on planes close to $\{10\bar{1}0\}$ or to (0001). To provide a graphical illustration of this stress state, we show the normal stress acting on given crystallographic planes (Figure 14), and the maximum resolved shear stress on those planes, for any plane orientation. Alternatively, the stress state inferred for MT can be represented as a Lamé stress ellipsoid (Figure 15 and Supplementary Movie S8). The stress ellipsoid is oblate in shape, with two principal stresses having similar absolute values (−4.4
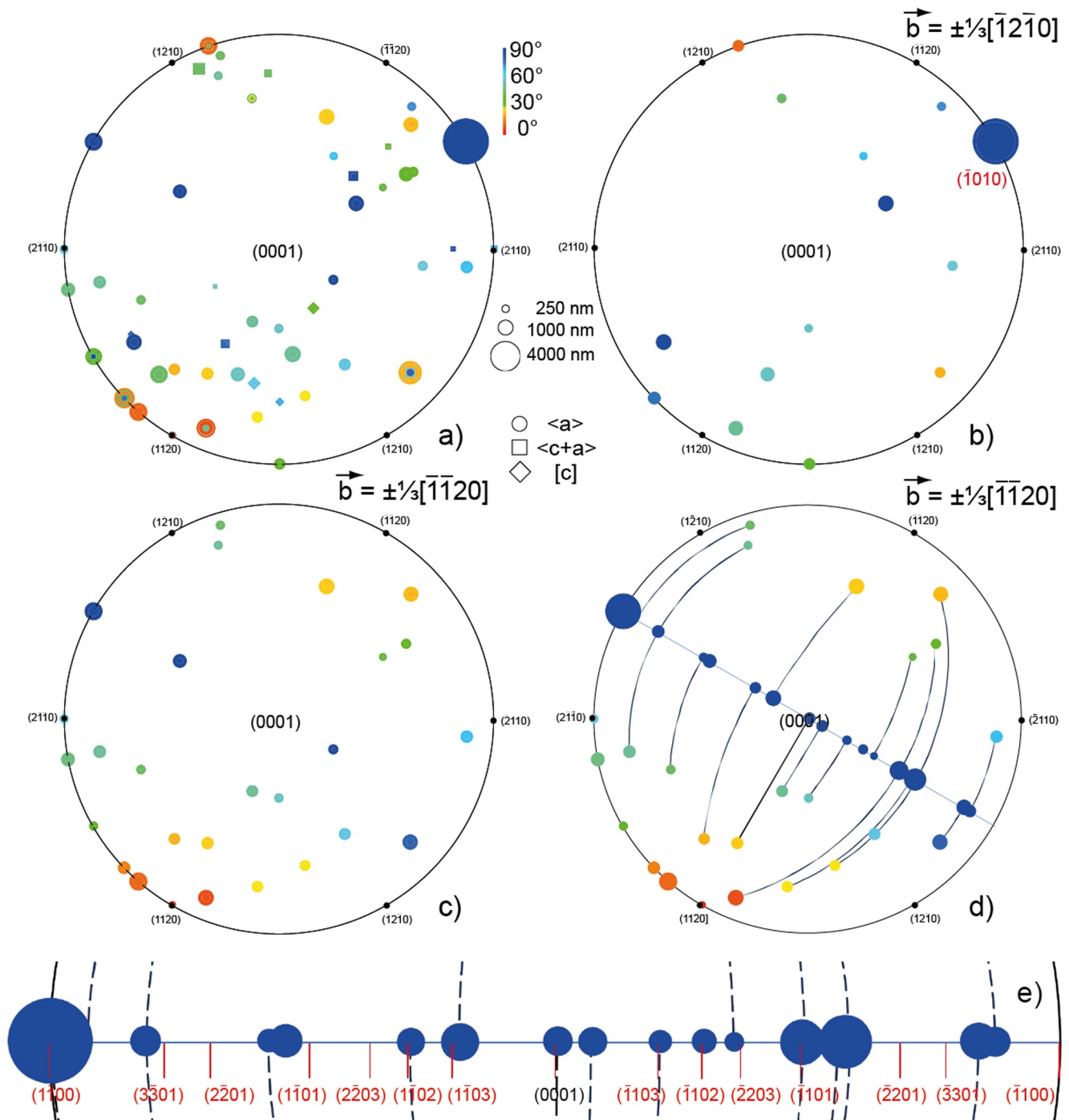
Figure 12. (0001) stereographic projection (upper hemisphere) of the normal to the habit planes of dislocations characterized in the main central thrust specimen. The rainbow color code is associated with the angle between the habit plane normal and the Burgers vectors (0° in red for pure climb and 90° in blue for glide) and the symbol sizes correspond to the lengths of dislocations using a non-linear scale illustrated by three examples: 250, 1,000 and 4,000 nm. (a) All observed Burgers vectors plotted ($\langle a \rangle$ dislocations are represented by circles, $\langle c + a \rangle$ by squares and $[c]$ by diamonds); (b) Projections of the habit plane normals for a_2 dislocations (a high proportion of dislocations are found in the $(\bar{1}010)$ glide plane); (c) Projections of the habit plane normal for a_3 dislocations (a few in glide planes and many in mixed climb configurations); (d) Stereographic projection for a_3 dislocations where the glide components of the mixed climb planes are extracted and added. These glide components are linked to their parent mixed climb plane by a solid line. (e) enlargement of the great circle of (d) showing glide planes normal to this plane. Labeled Miller indices of these planes show the diversity of glide components involved.
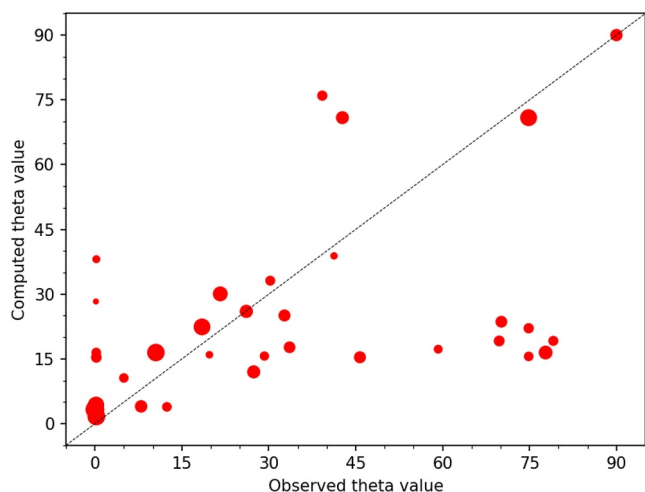
Figure 13. Computed θ^{mod} angles versus observed θ^{obs} angles after minimizing the objective function (Equation 12) to find the stress state at the time of deformation of the quartz grain of Moine Thrust specimen, that is most consistent with the observed dislocation segments. Each symbol corresponds to a different dislocation segment, and the symbol size is proportional to the segment length.

and 5.2) while the third one is significantly smaller (0.8). The stress ellipsoid, oriented along the TEM view direction, is represented in Figure 6a, and principal stresses are normalized by the critical shear stress for $\langle a \rangle$ glide.

While this estimation of the local stress state acting in situ does not take into account changes in stress during the plastic deformation history, it is, to our knowledge, the first estimation of in situ stress state based on observed dislocation structures. Moreover, the rheological coefficients thus obtained for MCT and MT shear zones correspond to in situ conditions and extremely slow geological strain-rates.

4.4. Limitations

Detailed TEM characterization of a mineral as electron-beam sensitive as quartz necessarily leads to a limited number of characterizations. Although statistical evaluation is difficult to apply, the validity of the results can be discussed from several points of view. While the analysis of the deformation microstructures of natural samples is of prime importance, it is not without its difficulties. The first is that these samples are the product of a long and complex history. We assume implicitly that the dislocations available for study at the end of deformation are comparable to (potentially exactly the same systems as) dislocations that were present and mobile during peak metamorphic and deformation conditions. For simple thermal histories, this assumption can be made as the exponential dependence of dislocation creep leads to an effective temperature when dislocation mobilities slow down and dislocations are left within the crystalline interior, much as the exponential dependence of diffusion can lead to effective closure temperatures that govern geochemical age determinations. In the case of this study, we do not seek to link microstructures or mechanisms to any particular moment of the sample deformation histories.

The question remains as to whether the microstructure active during deformation was erased by a late episode of recovery at low or negligible deviatoric stress, particularly since evidence of recovery (subgrain boundaries) is present. With regard to the major results of this study, specifically the widespread activation of $\langle c + a \rangle$ glide and the importance of mixed climb to dislocation creep, our conclusions do not depend on demonstrating their activity at peak metamorphic-tectonic conditions or the statistics of large numbers of observations. For example, the development of a dislocation loop in a mixed plane can only be understood in terms of simultaneous and equivalent glide and climb displacements. Such a microstructure cannot be the result of two distinct and successive episodes of deformation and recovery.
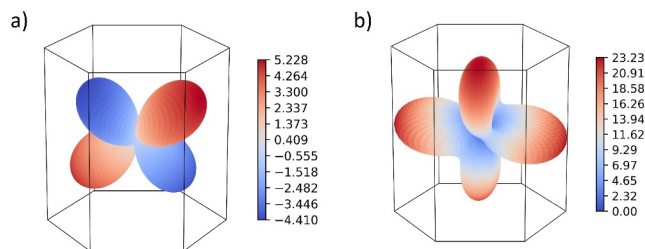
A highly focussed study such as ours also raises the question of whether it samples a representative volume element (RVE) which is the smallest volume over which a measurement can be made that will yield a value representative of the whole. As our study is based on a very small volume and a small number of dislocations, it is important to discuss the validity of our observations without the support of statistical elements. With regard to the observation of mixed climb, we emphasize that two grains from two distinct samples (to which we can add the granulite sample of Mussi, Gallet et al., 2021) lead to the same observation. This suggests that the crystalline defects of our studied volumes are not exceptional and that the conclusions drawn from these limited observations are probably more general in their significance.

The other result is the completeness of the plastic strain tensor, which leads to the conclusion that the von Mises criterion is satisfied. The volume sampled is surely not large enough to provide a quantitative measure of the plastic strain tensor for either shear zone, but the scale of study is sufficient to demonstrate that the necessary slip systems required to accommodate any general plastic strain were indeed activated.
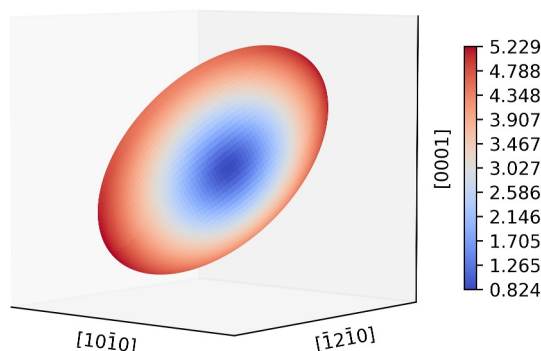

Figure 14. Stress state obtained for specimen Moine Thrust at the time of deformation after minimization of the objective function (Equation 12), plotted with respect to the hexagonal crystal lattice. (a) The normal stress acting on specific crystallographic planes, for any possible plane orientation (values normalized by the critical shear stress for $\langle a \rangle$ glide). (b) Shear stress acting on the same crystallographic planes (also normalized by the critical shear stress for $\langle a \rangle$ glide). For a stress tensor σ, the normal stress acting on a plane perpendicular to direction n is given by $\mathbf{n}.\sigma.\mathbf{n}$. The magnitude of the shear stress on that plane is $\|\sigma.\mathbf{n} - (\mathbf{n}.\sigma.\mathbf{n})\mathbf{n}\|$. The two plots show these two values for all possible orientations of $\mathbf{n}$ with respect to the hexagonal lattice. For example, the shear stress acting on the basal plane is large but the normal stress on the same plane is vanishingly small. Numerical stress values are dimensionless, normalized by the critical shear stress for $\langle a \rangle$ glide.

Figure 15. Lamé's stress ellipsoid with respect to crystallographic directions of the quartz grain of the Moine Thrust specimen. Among the three principal stresses, two have similar absolute values (-4.4 and 5.2) while the third one is significantly smaller (0.8) giving the ellipsoid an oblate shape. Stress values are relative, and dimensionless, normalized by the critical shear stress corresponding to $\langle a \rangle$ glide. See also Supplementary Movie S8.

We have also tried to deduce, from dislocation microstructures, the mechanical loading conditions acting at the crystal scale that may have generated the microstructures. Here, we exploit the highly anisotropic nature of crystalline plasticity. In the case of the MCT sample, we can see the difference in responses of dislocations a_2 and a_3 (Figure 12). The minimization of the objective function (Equation 12) gives the best results for the MT quartz grain, but it is unclear that this problem is uniquely solved. The local stress may include contributions from neighboring grains at the polycrystal scale, residual stresses of the dislocation network, and thermally derived stresses. Greater statistics would be required to capture the heterogeneity of stress in a polycrystalline rock over a much larger RVE.

5. Conclusion

Several important conclusions can be drawn from detailed 3D electron tomography of quartz specimens from the MCT and the MT, both of which were deformed extensively by dislocation creep in the presence of water. We show that $\langle a \rangle$ slip occurs predominantly on pyramidal and prismatic planes, that $\langle a \rangle$ basal glide is not active, and that [c] glide is not significant under those conditions. A remarkable new result of this study is the widespread activation of $\langle c + a \rangle$ glide in the $\{10\bar{1}0\}$, $\{10\bar{1}1\}$, $\{11\bar{2}n\}$ ($n = 1, 2$) and even $\{21\bar{3}1\}$ (not previously reported) planes. Even more remarkable is the conclusion that more than approximately 60% of all dislocations involve climb in their motion. This result could only be realized through characterization of the three-dimensional microstructure of the dislocation lines by electron tomography. The simultaneous motion of dislocations by glide and climb, known as mixed climb in materials science, is apparently widespread in naturally deformed quartz shear zones. This mode of deformation is characterized by displacement of dislocations in intermediate planes between the glide and climb planes, with significant implications for relative glide velocity v_g and climb velocity v_c; v_g and v_c must have comparable magnitudes under natural strain rates. Our quantitative characterization of slip systems in these samples demonstrates that glide of the observed dislocations can accommodate any arbitrary strain without strains due to climb, grain boundary sliding or other intercrystalline mechanisms. On the other hand, the magnitudes of strains achieved include significant contributions due to dislocation climb. Plastic strains produced by climb are not subordinate to those of glide; rather, they are of the same order of magnitude as strains due to glide (and possibly larger for the MCT specimen than for the lower temperature MT specimen). Strain analysis based on the exclusive activation of glide systems does not therefore provide a satisfactory description of quartz deformation at natural strain rates.

Data Availability Statement

Raw data are available at Zenodo repository (Weidner et al., 2024).

References

Baëta, R. D., & Ashbee, K. H. G. (1969). Slip systems in quartz: I experiments. *American Mineralogist*, *54*, 1551–1573.

Baëta, R. D., & Ashbee, K. H. G. (1973). Transmission electron microscopy studies of plastically deformed quartz. *Physica Status Solidi A*, *18*(1), 155–170. https://doi.org/10.1002/pssa.2210180112

Bakker, R. J., & Jansen, J. B. H. (1990). Preferential leakage from fluid inclusions by means of mobile dislocations. *Nature*, *345*(6270), 58–60. https://doi.org/10.1038/345058a0

Bakker, R. J., & Jansen, J. B. H. (1994). A mechanism for preferential H_2O leakage from fluid inclusions in quartz, based on TEM observations. *Contributions to Mineralogy and Petrology*, *116*(1–2), 7–20. https://doi.org/10.1007/bf00310686

Ball, A., & Glover, G. (1979). Dislocation climb deformation in quartz. *Bulletin de Mineralogie*, *102*(2), 188–194. https://doi.org/10.3406/bulmi.1979.7275

Ball, A., & White, S. (1978). On the deformation of quartzite. *Physics and Chemistry of Minerals*, *3*(2), 163–172. https://doi.org/10.1007/BF00308119

Barnard, J. S., Sharp, J., Tong, J. R., & Midgley, P. A. (2006). High-resolution three-dimensional imaging of dislocations. *Science*, *313*(5785), 319. https://doi.org/10.1126/science.1125783

Behrmann, J. H., & Mainprice, D. H. (1987). Deformation mechanisms in a high temperature quartz-feldspar mylonite: Evidence of superplastic flow in the lower continental crust. *Tectonophysics*, *140*(2–4), 297–305. https://doi.org/10.1016/0040-1951(87)90236-8

Blacic, J. D. (1975). Plastic deformation mechanisms in quartz: The effect of water. *Tectonophysics*, *27*(3), 271–294. https://doi.org/10.1016/0040-1951(75)90021-9

Boioli, F., Carrez, P., Cordier, P., Bevincre, B., & Marquille, M. (2015). Modeling the creep properties of olivine by 2.5-dimensional dislocation dynamics simulations. *Physical Review B*, *92*(1), 014115. https://doi.org/10.1103/PhysRevB.92.014115

Carrez, P., Mussi, A., & Cordier, P. (2024). On dislocation climb as an important deformation mechanism for planetary interiors. *Annual Review of Earth and Planetary Sciences*, *52*(1), 409–441. https://doi.org/10.1146/annurev-earth-031621-063108

Carter, N. L., Christie, J. M., & Griggs, D. T. (1964). Experimental deformation and recrystallization of quartz. *The Journal of Geology*, *72*(6), 687–733. https://doi.org/10.1086/627029

Castelnau, O., Derrien, K., Ritterbex, S., Carrez, P., Cordier, P., & Moulinec, H. (2020). Multiscale modeling of the effective viscoplastic behavior of Mg_2SiO_4 wadsleyite: Bridging atomic and polycrystal scales. *Comptes Rendus Mecanique*, *10–11*, 827–846. https://doi.org/10.5802/crmeca.61

Christie, J. M. (1960). Mylonitic rocks of the moine thrust zone in the Assynt region, north-west Scotland. *Transactions of the Geological Society of Edinburgh*, *18*(1), 79–93. https://doi.org/10.1144/transed.18.1.79

Christie, J. M. (1963). *The moine thrust zone in the Assynt region, northwest Scotland* (Vol. 40, pp. 345–440). University of California Publications in Geological Sciences. ISBN 9780598181923, 059818192X.

Christie, J. M., & Ardell, A. J. (1974). Substructures of deformation lamellae in quartz. *Geology*, *2*(8), 405–408. https://doi.org/10.1130/0091-7613(1974)2<405:SODLIQ>2.0.CO;2

Christie, J. M., & Ardell, A. J. (1976). Deformation structures in minerals. In H. R. Wenk (Ed.), *Electron microscopy in mineralogy*. Springer. https://doi.org/10.1007/978-3-642-66196-9_29

Christie, J. M., Heard, H. C., & LaMori, P. N. (1964). Experimental deformation of quartz single crystals at 27 to 30 kilo bars confining pressure and 24°C. *American Journal of Science*, *262*(1), 26–55. https://doi.org/10.2475/ajs.262.1.26

Christie, J. M., McIntyre, D. B., & Weiss, L. E. (1954). *Appendix to McIntyre, D.B., the moine thrust – its discovery, age and tectonic significance* (Vol. 65, pp. 219–220). Proceedings of the Geologists' Association. https://doi.org/10.1016/S0016-7878(54)80042-3

Cordier, P., Boulogne, P., & Doukhan, J. C. (1988). Water precipitation and diffusion in wet quartz and wet berlinite $AlPO_4$. *Bulletin de Mineralogie*, *111*(2), 113–137. https://doi.org/10.3406/bulmi.1988.8077

Cordier, P., & Doukhan, J. C. (1989). Water solubility in quartz and its influence on ductility. *European Journal of Mineralogy*, *1*(2), 221–237. https://doi.org/10.1127/ejm/1/2/0221

Cordier, P., & Doukhan, J.-C. (1991). Water speciation in quartz: A near infrared study. *American Mineralogist*, *76*, 361–369.

Cotton, J. D., Kaufman, M. J., & Noebe, R. (1991). A simplified method for determining the number of independent slip systems in crystals. *Scripta Metallurgica et Materialia*, *25*(10), 2395–2398. https://doi.org/10.1016/0956-716X(91)90036-Z

Couret, A. (2010). Low and high temperature deformation mechanisms in TiAl Alloys. *Journal of Physics: Conference Series*, *240*, 012001. https://doi.org/10.1088/1742-6596/240/1/012001

De Ridder, R., & Amelinckx, S. (1971). Approximate theoretical treatment of weak-beam dislocation images. *Physica Status Solidi*, *43*(2), 541–550. https://doi.org/10.1002/pssb.2220430211

Doukhan, J.-C., & Paterson, M. S. (1986). Solubility of water in quartz - A revision. *Bulletin de Mineralogie*, *109*(3), 193–198. https://doi.org/10.3406/bulmi.1986.7928

Doukhan, J. C., & Trépied, L. (1985). Plastic deformation of quartz single crystals. *Bulletin de Mineralogie*, *108*(1), 97–123. https://doi.org/10.3406/bulmi.1985.7860

Faleiros, F. M., Moraes, R., Pavan, M., & Campanha, G. A. C. (2016). A new empirical calibration of the quartz c-axis fabric opening-angle deformation thermometer. *Tectonophysics*, *671*, 173–182. https://doi.org/10.1016/j.tecto.2016.01.014

Fliervoet, T., White, S., & Drury, M. R. (1997). Evidence for dominant grain-boundary sliding deformation in greenschist-and amphibole-grade polymineralic ultra mylonites from the redbank deformed zone, Central Australia. *Journal of Structural Geology*, *19*(12), 1495–1520. https://doi.org/10.1016/S0191-8141(97)00076-X

Francsis, M. K. (2012). *Piezometry and strain rate estimates along mid-crustal shear zones*. Unpublished MS thesis. Virginia Tech. https://vtechworks.lib.vt.edu/handle/10919/32170

Fukuda, J.-I., Holyoke III, C. W., & Kronenberg, A. K. (2018). Deformation of fine-grained quartz aggregates by mixed diffusion and dislocation creep. *Journal of Geophysical Research: Solid Earth*, *123*(6), 4676–4696. https://doi.org/10.1029/2017JB015133

Galy, B., Musi, M., Hantcherli, M., Molénat, G., Couret, A., Spoerk-Erdely, P., et al. (2023). Glide and mixed climb dislocation velocity in γ-TiAl investigated by in-situ transmission electron microscopy. *Scripta Materialia*, *228*, 115333. https://doi.org/10.1016/j.scriptamat.2023.115333

Gerretsen, J., Paterson, M. S., & McLaren, A. C. (1989). The uptake and solubility of water in quartz at elevated pressure and temperature. *Physics and Chemistry of Minerals*, *16*(4), 334–342. https://doi.org/10.1007/BF00199553

Griggs, D. (1967). Hydrolytic weakening of quartz and other silicates. *Geophysical Journal International*, *14*(1–4), 19–31. https://doi.org/10.1111/j.1365-246X.1967.tb06218.x

Griggs, D. (1974). A model of hydrolytic weakening in quartz. *Journal of Geophysical Research*, *79*(11), 1653–1661. https://doi.org/10.1029/JB079i011p01653

Griggs, D. T., & Blacic, J. D. (1965). Quartz: Anomalous weakness of synthetic crystals. *Science*, *147*(3655), 292–295. https://doi.org/10.1126/science.147.3655.292

Hata, S., Miyazaki, H., Miyazaki, S., Mitsuhara, M., Tanaka, M., Kaneko, K., et al. (2011). High-angle triple-axis specimen holder for three-dimensional diffraction contrast imaging in transmission electron microscopy. *Ultramicroscopy*, *111*(8), 1168–1175. https://doi.org/10.1016/j.ultramic.2011.03.021

Heard, H. C., & Carter, N. L. (1968). Experimentally induced "natural" intragranular flow in quartz and quartzite. *American Journal of Science*, *266*, 1–42. https://doi.org/10.2475/ajs.266.1.1

Heggie, M. (1992). A molecular water pump in quartz dislocations. *Nature*, *355*(6358), 337–339. https://doi.org/10.1038/355337a0

Heggie, M., & Jones, R. (1986). Models of hydrolytic weakening in quartz. *Philosophical Magazine A*, *53*(5), L65–L70. https://doi.org/10.1080/01418618608242857

Heggie, M., Jones, R., & Nylen, M. (1985). Electronic structure of α-quartz, the [1010] surface and perfect stoichiometric dislocations. *Philosophical Magazine B*, *51*(6), 573–580. https://doi.org/10.1080/13642818508243148

Herman, G. T., Lakshminarayanan, A. V., & Naparstek, A. (1976). Convolution reconstruction techniques for divergent beams. *Computers in Biology and Medicine*, *6*(4), 259–271. https://doi.org/10.1016/0010-4825(76)90065-2

Hirsch, P. B. (1981). Plastic deformation and electronic mechanisms in semiconductors and insulators. *Journal de Physique. Colloques*, *42*(C3), 149–160. https://doi.org/10.1051/jphyscol:1981313

Hirth, G., Teyssier, C., & Dunlap, W. J. (2001). An evaluation of quartzite flow laws based on comparisons between experimentally and naturally deformed rocks. *International Journal of Earth Sciences*, *90*(1), 77–87. https://doi.org/10.1007/s005310000152

Hirth, G., & Tullis, J. (1992). Dislocation creep regimes in quartz aggregates. *Journal of Structural Geology*, *14*(2), 145–159. https://doi.org/10.1016/0191-8141(92)90053-Y

Hobbs, B. E. (1968). Recrystallization of single crystals of quartz. *Tectonophysics*, *6*(5), 353–401. https://doi.org/10.1016/0040-1951(68)90056-5

Hobbs, B. E. (1981). The influence of metamorphic environment upon the deformation of minerals. *Tectonophysics*, *78*(1–4), 335–383. https://doi.org/10.1016/0040-1951(81)90020-2

Hobbs, B. E. (1984). Point defect chemistry of minerals under a hydrothermal environment. *Journal of Geophysical Research*, *89*(B6), 4026–4038. https://doi.org/10.1029/JB089iB06p04026

Hodges, K. V. (2000). Tectonic of the Himalaya and southern Tibet from two perspectives. *Geological Society of America Bulletin*, *112*(3), 324–350. https://doi.org/10.1130/0016-7606(2000)112<324:TOTHAS>2.0.CO;2

Holyoke, C. W., III, & Kronenberg, A. K. (2010). Accurate differential stress measurement using the molten salt cell and solid salt assemblies in the Griggs apparatus with application to strength, piezometers and rheology. *Tectonophysics*, *494*(1–2), 17–31. https://doi.org/10.1016/j.tecto.2010.08.001

Ishida, Y., Ishida, H., Kohra, K., & Ichinose, H. (1980). Determination of the Burgers vector of a dislocation by weak-beam imaging in a HVEM. *Philosophical Magazine A*, *42*(4), 453–462. https://doi.org/10.1080/01418618008239369

Johnson, M. R. W., Kelley, S. P., Oliver, G. J. H., & Winter, D. A. (1985). Thermal effects and timing of thrusting in the moine thrust zone. *Journal Geological Society London*, *142*(5), 863–873. https://doi.org/10.1144/gsjgs.142.5.0863

Kekulawala, K. R. S. S., Paterson, M. S., & Boland, J. N. (1978). Hydrolytic weakening in quartz. *Tectonophysics*, *46*(1–2), T1–T6. https://doi.org/10.1016/0040-1951(78)90101-4

Kekulawala, K. R. S. S., Paterson, M. S., & Boland, J. N. (1981). An experimental study of the role of water in quartz deformation. In N. L. Carter, M. Friedman, J. M. Logan, & D. W. Stearns (Eds.), *Mechanical behavior of crustal rocks (the Handin volume), geophysical monograph* (Vol. 24, pp. 49–60). Amer. Geophys. Union. https://doi.org/10.1029/gm024p0049

Keller, L. M., & Stipp, M. (2011). The single-slip hypothesis revisited: Crystal-preferred orientations of sheared quartz aggregates with increasing strain in nature and numerical simulation. *Journal of Structural Geology*, *33*(10), 1491–1500. https://doi.org/10.1016/j.jsg.2011.07.008

Kirby, S. H., & McCormick, K. W. (1979). Creep of hydrolytically weakened synthetic quartz crystals oriented to promote {2-1-10} <0001> slip: A brief summary of work to date. *Bulletin de Mineralogie*, *102*(2), 124–137. https://doi.org/10.3406/bulmi.1979.7265

Kronenberg, A. K., Ashley, K. T., Francsis, M. K., Holyoke III, C. W., Jezek, L., Kronenberg, J. A., et al. (2020). Water loss during dynamic recrystallization of moine thrust quartzites, northwest Scotland. *Geology*, *48*(6), 557–561. https://doi.org/10.1130/G47041.1

Kronenberg, A. K., Hasnan, H. F. B., Holyoke III, C. W., Law, R. D., Liu, Z., & Thomas, J. B. (2017). Synchrotron FTIR imaging of OH in quartz mylonites. *Solid Earth*, *8*(5), 1025–1045. https://doi.org/10.5194/se-8-1025-2017

Kronenberg, A. K., Kirby, S. H., Aines, R. D., & Rossman, G. R. (1986). Solubility and diffusional uptake of hydrogen in quartz at high water pressures: Implications for hydrolytic weakening. *Journal of Geophysical Research*, *91*(B12), 12723–12744. https://doi.org/10.1029/JB091iB12p12723

Kruhl, J. (1998). Reply: Prism- and basal-plane parallel subgrain boundaries in quartz: A microstructural geothermobarometer. *Journal of Metamorphic Geology*, *16*, 142–146.

Law, R. D. (2014). Deformation thermometry based on quartz c-axis fabrics and recrystallization microstructures: A review. *Journal of Structural Geology*, *66*, 129–161. https://doi.org/10.1016/j.jsg.2014.05.023

Law, R. D., Casey, M., & Knipe, R. J. (1986). Kinematic and tectonic significance of microstructures and crystallographic fabrics within quartz mylonites from the Assynt and Eriboll regions of the moine thrust zone, NW Scotland. *Transactions of the Royal Society of Edinburgh Earth Sciences*, *77*(2), 99–125. https://doi.org/10.1017/S0263593300010774

Law, R. D., & Johnson, M. R. W. (2010). Microstructures and crystal fabrics of the moine thrust zone and moine nappe: History of research and changing tectonic interpretations. *Geological Society, London, Special Publications*, *335*(1), 443–503. https://doi.org/10.1144/SP335.21

Law, R. D., Mainprice, D., Casey, M., Lloyd, G. E., Knipe, R. J., Cook, B., & Thigpen, J. R. (2010). Moine thrust zone mylonites at the Stack of Glencoul: 1 - Microstructures, strain and influence of recrystallization on quartz crystal fabric development. *Geological Society, London, Special Publications*, *335*, 543–577. https://doi.org/10.1144/SP335.23

Law, R. D., Stahr, D. W., III, Francsis, M. K., Ashley, K. T., Grasemann, B., & Ahmad, T. (2013). Deformation temperatures and flow vorticities near the base of the Himalayan Series, Sutlej Valley and Shimla Klippe, NW India. *Journal of Structural Geology*, *54*, 21–53. https://doi.org/10.1016/j.jsg.2013.05.009

Lebensohn, R. A., Hartley, C. S., Tomé, C. N., & Castelnau, O. (2010). Modelling the mechanical response of polycrystals deforming by climb and glide. *Philosophical Magazine*, *90*(5), 567–583. https://doi.org/10.1080/14786430903213320

Lister, G. S., & Hobbs, B. E. (1980). The simulation of fabric development during plastic deformation and its application to quartzite: The influence of deformation history. *Journal of Structural Geology*, *2*(3), 355–370. https://doi.org/10.1016/0191-8141(80)90023-1

Liu, G. S., & Robertson, I. M. (2011). Three-dimensional visualization of dislocation-precipitate interactions in a Al–4Mg–0.3Sc alloy using weak-beam dark-field electron tomography. *Journal of Materials Research*, *26*(4), 514–522. https://doi.org/10.1557/jmr.2010.83

Madec, R., Devincre, B., Kubin, L., Hoc, T., & Rodney, D. (2003). The role of collinear interaction in dislocation-induced hardening. *Science*, *301*(5641), 1879–1882. https://doi.org/10.1126/science.1085477

Mainprice, D., Bouchez, J. L., Blumenfeld, P., & Tubià, J. M. (1986). Dominant c slip in naturally deformed quartz: Implications for dramatic plastic softening at high temperature. *Geology*, *14*(10), 819–822. https://doi.org/10.1130/0091-7613(1986)14<819:DCSIND>2.0.CO;2

Malaplate, J., Caillard, D., & Couret, A. (2004). Interpretation of the stress dependence of creep by a mixed climb mechanism in TiAl. *Philosophical Magazine*, *84*(34), 3671–3687. https://doi.org/10.1080/14786430412331284009

McLaren, A. C., Fitz Gerald, J. D., & Gerretsen, J. (1989). Dislocation nucleation and multiplication in synthetic quartz: Relevance to water weakening. *Physics and Chemistry of Minerals*, *16*(5), 465–482. https://doi.org/10.1007/BF00197016

McLaren, A. C., & Hobbs, B. E. (1972). Transmission electron microscope investigation of some natural deformed quartzites. In H. C. Heard, I. Y. Borg, N. L. Carter, & C. B. Raleigh (Eds.), *Flow and fracture of rocks* (Vol. 16, pp. 55–66). American Geophysical Union, Geophysical Monograph Series. https://doi.org/10.1029/GM016p0055

Messaoudi, C., Boudier, T., Sanchez Sorzano, C. O., & Marco, S. (2007). TomoJ: Tomography software for three-dimensional reconstruction in transmission electron microscopy. *BMC Bioinformatics*, *8*(1), 288. https://doi.org/10.1186/1471-2105-8-288

Morales, L. F. G., Lloyd, G. E., & Mainprice, D. (2014). Fabric transitions in quartz via viscoplastic self-consistent modeling part I: Axial compression and simple shear under constant strain. *Tectonophysics*, *636*, 52–69. https://doi.org/10.1016/j.tecto.2014.08.011

Morales, L. F. G., Mainprice, D., Lloyd, G. E., & Law, R. D. (2011). Crystal fabric development and slip systems in a quartz mylonite: An approach via transmission electron microscopy and viscoplastic self-consistent modelling. *Geological Society, London, Special Publications*, *360*(1), 151–174. https://doi.org/10.1144/SP360.9

Morniroli, J. P., Vankieken, D., & Winter, L. (1994). *Electron diffraction. Dedicated software to kinematicaly simulate CBED patterns*. USTL, Lille).

Morrison-Smith, D. J., Paterson, M. S., & Hobbs, B. E. (1976). An electron microscope study of plastic deformation in single crystals of synthetic quartz. *Tectonophysics*, *33*(1–2), 43–79. https://doi.org/10.1016/0040-1951(76)90051-2

Mussi, A., Carrez, P., Gouriet, K., Hue, B., & Cordier, P. (2021). 4D electron tomography of dislocations undergoing electron irradiation. *Comptes Rendus Physique*, *22*(S3), 67–81. https://doi.org/10.5802/crphys.80

Mussi, A., Cordier, P., & Demouchy, S. (2015). Characterization of dislocation interactions in olivine using electron tomography. *Philosophical Magazine*, *95*(4), 335–345. https://doi.org/10.1080/14786435.2014.1000996

Mussi, A., Cordier, P., Demouchy, S., & Hue, B. (2017). Hardening mechanisms in olivine single crystal deformed at 1090°C: An electron tomography study. *Philosophical Magazine*, *97*(33), 3172–3185. https://doi.org/10.1080/14786435.2017.1367858

Mussi, A., Cordier, P., Ghosh, S., Garvik, N., Nzogang, B. C., Carrez, P., & Garruchet, S. (2016). Transmission electron microscopy of dislocations in cementite deformed at high pressure and high temperature. *Philosophical Magazine*, *96*(17), 1773–1789. https://doi.org/10.1080/14786435.2016.1177700

Mussi, A., Gallet, J., Castelnau, O., & Cordier, P. (2021). Application of electron tomography of dislocations in beam-sensitive quartz to the determination of strain components. *Tectonophysics*, *803*, 228754. https://doi.org/10.1016/j.tecto.2021.228754

Nabarro, F. R. N. (1967). Steady-state diffusional creep. *Philosophical Magazine A*, *16*(140), 231–237. https://doi.org/10.1080/14786436708229736

Okudaira, T., Takeshita, T., Hara, I., & Ando, J.-I. (1995). A new estimate of the conditions for transition from basal <a> to prism [c] slip in naturally deformed quartz. *Tectonophysics*, *250*(1–3), 31–46. https://doi.org/10.1016/0040-1951(95)00039-4

Ord, A., & Christie, J. M. (1984). Flow stresses from microstructures in mylonitic quartzites of the moine thrust zone, Assynt area, Scotland. *Journal of Structural Geology*, *6*, 639–654. https://doi.org/10.1016/0191-8141(84)90002-6

Pettersen, E. F., Goddard, T. D., Huang, C. C., Couch, G. S., Greenblatt, D. M., Meng, E. C., & Ferrin, T. E. (2004). UCSF Chimera: A visualization system for exploratory research and analysis. *Journal of Computational Chemistry*, *25*(13), 1605–1612. https://doi.org/10.1002/jcc.20084

Rutter, E. H., & Brodie, K. H. (2004). Experimental grain size-sensitive flow of hot-pressed Brazilian quartz aggregates. *Journal of Structural Geology*, *26*(11), 2011–2023. https://doi.org/10.1016/j.jsg.2004.04.006

Stipp, M., Stünitz, H., Heilbronner, R., & Schmid, S. M. (2002b). Dynamic recrystallization of quartz: Correlation between natural and experimental conditions. *Geological Society, London, Special Publications*, *200*(1), 171–190. https://doi.org/10.1144/GSL.SP.2001.200.01.11

Stipp, M., Stünitz, H., Heilbronner, R., & Schmid, S. (2002a). The eastern Tonale fault zone: A natural laboratory for crystal plastic deformation of quartz over a temperature range from 250 to 700°C. *Journal of Structural Geology*, *24*(12), 1861–1884. https://doi.org/10.1016/S0191-8141(02)00035-4

Stipp, M., Tullis, J., & Behrens, H. (2006). Effect of water on the dislocation creep microstructure and flow stress of quartz and implications for the recrystallized grain size piezometer. *Journal of Geophysical Research*, *111*(B4), 201–220. https://doi.org/10.1029/2005JB003852

Strachan, R. A., Smith, M., Harris, A. L., & Fettes, D. J. (2002). The Northern Highland and Grampian Terranes. In N. H. Trewin (Ed.), *The Geology of Scotland* (pp. 81–147). The Geological Society.

Sylvester, A. G. (1969). A microfabric study of calcite, dolomite, and quartz around Papoose Flat Pluton, California. *Geological Society of America Bulletin*, *80*(7), 1311–1328. https://doi.org/10.1130/0016-7606(1969)80[1311:SMSOCD]2.0.CO;2

Taylor, G. I. (1938). Plastic strain in metals. *Journal of the Institute of Metals*, *62*, 307–324.

Tokle, L., Hirth, G., & Behr, W. M. (2019). Flow laws and fabric transitions in wet quartzite. *Earth and Planetary Science Letters*, *505*, 152–161. https://doi.org/10.1016/j.epsl.2018.10.017

Trépied, L., & Doukhan, J. C. (1982). Evidence of ⟨a + c⟩ dislocations in synthetic quartz single crystals compressed along the c axis. *Bulletin de Minéralogie*, *105*(2), 176–180. https://doi.org/10.3406/bulmi.1982.7601

Trepmann, C. A., & Stöckhert, B. (2003). Quartz microstructures developed during non-steady state plastic flow at rapidly decaying stress and strain rate. *Journal of Structural Geology*, *25*(12), 2035–2051. https://doi.org/10.1016/S0191-8141(03)00073-7

Trepmann, C. A., & Stöckhert, B. (2013). Short-wavelength undulatory extinction in quartz recording coseismic deformation in the middle crust – An experimental study. *Solid Earth*, *4*(2), 263–276. https://doi.org/10.5194/se-4-263-2013

Tullis, J., Christie, J. M., & Griggs, D. T. (1973). Microstructures and preferred orientations of experimentally deformed quartzites. *GSA Bulletin*, *84*(1), 297–314. https://doi.org/10.1130/0016-7606(1973)84%3C297:MAPOOE%3E2.0.CO;2

Tullis, J., & Yund, R. A. (1989). Hydrolytic weakening of quartz aggregates: The effect of water and pressure on recovery. *Geophysical Research Letters*, *16*(11), 1343–1346. https://doi.org/10.1029/GL016i011p01343

Vernooij, M. G. C. (2005). *Dynamic recrystallisation and microfabric development in single crystals of quartz during experimental deformation*. Ph.D. thesis (Vol. 16050, p. 128). ETH Zürich, Nr. http://e-collection.ethbib.ethz.ch/show?type=diss&nr=16050

Voisin, T., Monchoux, J. P., Thomas, M., Deshayes, C., & Couret, A. (2016). Mechanical properties of the TiAl IRIS alloy. *Metallurgical and Materials Transactions A*, *47*(12), 6097–6108. https://doi.org/10.1007/s11661-016-3801-3

von Mises, R. (1928). Mechanik der plastischen Form¨anderung von Kristallen. *Zeitschrift für Angewandte Mathematik und Mechanik*, *8*(3), 161–185. https://doi.org/10.1002/zamm.19280080302

Wallis, D., Parsons, A. J., & Hansen, L. N. (2019). Quantifying geometrically necessary dislocations in quartz using HR-EBSD: Application to chessboard subgrain boundaries. *Journal of Structural Geology*, *125*, 235–247. https://doi.org/10.1016/j.jsg.2017.12.012

Weathers, M. S., Bird, J. M., Cooper, R. F., & Kohlstedt, D. L. (1979). Differential stress determined from deformation-induced microstructures of the Moine thrust zone. *Journal of Geophysical Research*, *84*(B13), 7495–7509. https://doi.org/10.1029/JB084iB13p07495

Weertman, J. (1968). Dislocation climb theory of steady-state creep. *Transactions of the American Society of Metals*, *61*, 681–694.

Weidner, T., Mussi, A., Castelnau, O., Kronenberg, A., Law, R., & Cordier, P. (2024). Research data supporting "evidence of dislocation mixed climb in quartz from the moine and Main Central thrusts: An electron tomography study". [Dataset]. *Zenodo*. https://doi.org/10.5281/zenodo.10635128

Wenk, H.-R., Canova, G., Molinari, A., & Kocks, U. F. (1989). Viscoplastic modelling of texture development in quartzite. *Journal of Geophysical Research*, *94*(B12), 17895–17906. https://doi.org/10.1029/JB094iB12p17895

Wenk, H.-R., Yu, R., Vogel, S., & Vasin, R. (2019). Preferred orientation of quartz in metamorphic rocks from the Bergell Alps. *Minerals*, *9*(5), 1–35. https://doi.org/10.3390/min9050277

White, S. (1977). Geological significance of recovery and recrystallization processes in quartz. *Tectonophysics*, *39*(1–3), 143–170. https://doi.org/10.1016/0040-1951(77)90093-2

Yuan, S., Huang, M., Zhu, Y., & Li, Z. (2018). A dislocation climb/glide coupled crystal plasticity constitutive model and its finite element implementation. *Mechanics of Materials*, *118*, 44–61. https://doi.org/10.1016/j.mechmat.2017.12.009